TECHNISCHE
UNIVERSITÄT
WIEN
Vienna University of Technology

Diplomarbeit

Dissipation and Fluctuations

Investigation of Anchor Losses for Micromechanical Plate Resonators

zur Erlangung des akademischen Grades

Diplom-Ingenieur/in

im Rahmen des Studiums

066/460 Physikalische Energie- und Messtechnik

eingereicht von

Marco Stixenberger

Matrikelnr.: 01225270

Ausgeführt am
Institut für Sensor- und Aktuatorsysteme
der Technischen Universität Wien

Betreuung
Univ.Prof. Dipl.-Phys. Dr.rer.nat. Ulrich Schmid
Dr. Daniel Platz
André Loch Gesing

Wien, 10.01.2022   _____   _____
                                 Unterschrift   Unterschrift
                               Verfasser/in   Betreuer/in

Abstract

Micromechanical resonators are crucial components of various sensing devices, and their performance is limited by different sources of damping. In this work, we investigate so-called anchor losses, where energy is lost due to the propagation of elastic waves from the resonator to the elastic substrate. These type of losses are a dominant source of damping for MEMS devices in vacuum. There are several existing analytical and numerical studies to estimate the quality factor of slendered, isotropic beams. In our approach, we go one step beyond and design a finite-element model to investigate the behavior of anchor losses for higher-order modes of rectangular shaped plate-resonators. Additionally, we show that the anchor loss related quality factor (and thus the energy loss to the environment) for two-dimensional modes is affected by interference phenomena in the substrate, which results in a modulation of the quality factor by up to two orders of magnitude with varying plate width. To validate our results, we design and fabricate plate resonators with different widths, measure their quality factors using laser-doppler vibrometry and compare them to the numerical estimations. The measured quality factors are in good agreement with the numerical values.

Deutsche Kurzfassung

Mikromechanische Resonatoren spielen eine entscheidende Rolle beim Design verschiedenster Sensoren. Die fundamentalen Leistungsgrenzen dieser Sensoren sind im Allgemeinen durch verschiedene Dämpfungseffekte bestimmt. Diese Arbeit konzentriert sich auf sogenannte *Anchor Losses*, bei denen Energie durch die Ausbreitung elastischer Wellen vom Resonator in die Umgebung verloren geht. Diese Art von Verlusten ist ein dominierender Faktor für MEMS-Sensoren in Vakuum. Mehrere analytische und numerische Studien beschäftigen sich mit der Abschätzung des Gütefaktors schmaler, isotroper Balken. Die vorliegende Arbeit geht einen Schritt weiter, und versucht das Verhalten von Ankerverlusten für Moden höherer Ordnung von Plattenresonatoren zu beschreiben. Darüber hinaus wird gezeigt, dass der mit dem Ankerverlust verbundene Gütefaktor (und damit der Energieverlust in die Umgebung) für bestimmte zweidimensionale Moden durch Interferenzeffekten im Substrat beeinflusst wird. Zum Validieren der numerischen Resultate wurden unterschiedlichste Designs von Plattenresonatoren entworfen und gefertigt. Der jeweilige Gütefaktor wurden dann unter Verwendung von Laser-Doppler-Vibrometrie bestimmt und mit den numerischen Ergebnissen verglichen. Die experimentellen Ergebnisse zeigen Variationen des Quality Factors in ähnlicher Größenordnung wie von den numerischen Ergebnissen vorhergesagt.

Acknowledgment

First, I want to thank Professor Ulrich Schmid for giving me the opportunity to do my master's project at his group.

Special thanks go to my supervisors Daniel Platz and André Loch Gesing, for hundreds of hours of fruitful discussions and many encouraging words.

Additionally, I want to thank Hendrik Kähler for his help with the finite-element model, and Ioan Ignat for his support with fabrication and experiments.

Hiermit erkläre ich, dass die vorliegende Arbeit gemäß dem Code of Conduct – Regeln zur Sicherung guter wissenschaftlicher Praxis (in der aktuellen Fassung des jeweiligen Mitteilungsblattes der TU Wien), insbesondere ohne unzulässige Hilfe Dritter und ohne Benutzung anderer als der angegebenen Hilfsmittel, angefertigt wurde. Die aus anderen Quellen direkt oder indirekt übernommenen Daten und Konzepte sind unter Angabe der Quelle gekennzeichnet. Die Arbeit wurde bisher weder im In– noch im Ausland in gleicher oder in ähnlicher Form in anderen Prüfungsverfahren vorgelegt.

<div style="margin-top:3em"></div>

_____   _____
Ort, Datum   Marco Stixenberger

Contents

1. Introduction

Resonant micro-sensors and micro-actuators, based on microelectromechanical systems (MEMS) technology, are a recent success story which paved the way for a wide range of applications, e.g. atomic force microscopy [1], energy harvesting [2], viscosity sensors [3] and micro-fluidic-pumps [4].

A key performance aspect of any sensor (macro and micro) is its sensitivity, which determines the minimum detectable signal. From the fluctuation-dissipation theorem[1], we know that the mechanisms that give rise to noise (fluctuation) in any continuous system in thermal equilibrium are linked to dissipation mechanisms. Dissipation mechanisms directly influence the usability of micromechanical resonators for sensing devices or other applications.

For resonating MEMS devices, the most dominant loss mechanisms are losses to the surrounding medium (acoustic and viscous losses), surface losses, intrinsic material losses, thermoelastic damping (TED) losses and anchor losses [6]. The damping is quantified by the quality factor Q, which is defined by dividing the energy stored in the system by the energy dissipated per vibration cycle:

$$Q = 2\pi \cdot \frac{E_{\text{stored}}}{\Delta W} \tag{1}$$

When a resonating system is excited in the linear regime (which is usually the case for small amplitudes), it can be approximated by a harmonic oscillator. Using this simplification, the quality factor can be identified in the harmonic oscillator's equation of motion (see Appendix A.2):

$$Q = \frac{1}{2\zeta} \tag{2}$$

ζ is the damping ratio of the oscillator, and is related to the spring constant k, the damping constant c and the oscillating mass m by the following expression:

$$\zeta = \frac{c}{2\sqrt{mk}} \tag{3}$$

Using this approximation, Q is inversely proportional to the width of the resonance peak and enables the estimation of the quality factor by measuring the resonance bandwidth of a vibrational mode. For resonators used in sensor- or filter applications, high quality factors are usually desired, as a high quality factor increases the signal-to-noise ratio (SNR)[2]. The total quality factor Q_{tot} of a system can be determined by adding up the reciprocal quality factors of the individual loss mechanisms [6]:

---

[1]Fluctuation-Dissipation-Theorem: For every process that dissipates energy, there is a reverse process related to thermal fluctuations. First described by Einstein in 1905 [5].

[2]The quality factor of a resonating system is inversely proportional to its phase noise. This is described by Leeson's equation [7].

$$\frac{1}{Q_{\text{tot}}} = \frac{1}{Q_{\text{medium}}} + \frac{1}{Q_{\text{clamping}}} + \frac{1}{Q_{\text{intrinsic}}} + \frac{1}{Q_{\text{other}}} \tag{4}$$

For MEMS resonators placed in vacuum, medium losses do not exist and other loss mechanisms dominate. The thickness of micromechanical resonators typically ranges from 1 µm to 50 µm. In this range, anchor- [2] and thermoelastic losses dominate over surface and material losses, so the total energy loss is mostly a combination of anchor and TED losses [6]. Understanding and minimizing TED and anchor losses in MEMS is an area of intense research. There have been several analytical [8] [9], and numerical studies [10] [11] on the effects of anchor losses for slender and isotropic beam resonators. In this work, we extend this analysis to the effects of 2D-modes[3] of plate resonators. As the shape of these modes can form very complex patterns, the local force distribution in the anchor is also much more complex than for 1D-modes of beam resonators. This is illustrated in Figure 1, where the stress distribution in the anchor is shown for a beam resonator vibrating in its first bending mode, and a plate resonator vibrating in a higher order plate mode.

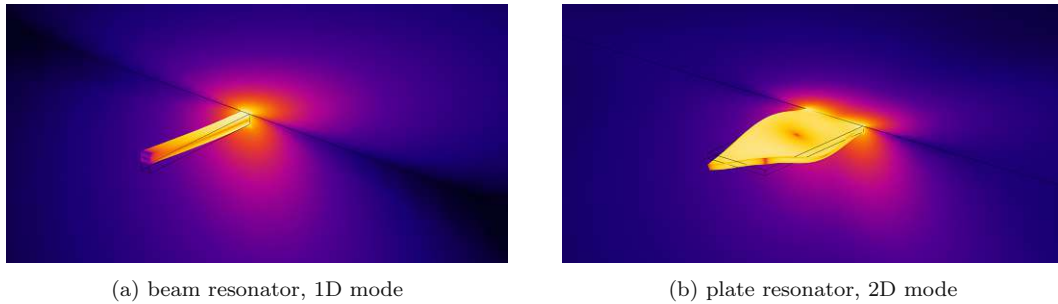(a) beam resonator, 1D mode   (b) plate resonator, 2D mode

Figure 1: Illustration of the stress distribution in the anchor for two different resonators. The resonators are attached to the edge of a substrate, which is acting as a sink for elastic wave energy. The stress level is especially high at the intersection between resonator and substrate, and declines with increasing distance from the resonator. Dependent on the vibrational mode, complex stress patterns are formed in the anchor region. (a) long, slender beam resonator vibrating in its fundamental bending mode. (b) plate resonator vibrating in a 2D plate-mode. Colors are not to scale.

A novel approach to reduce anchor losses are *phononic crystals* [12]. A phononic crystal exhibits a periodic pattern of holes. For specific arrangements of these holes, the acoustic band diagram features band gaps, i.e. elastic waves with frequencies inside the band gap cannot propagate through the phononic crystal. This band gap allows the use of phononic band gaps to block the energy flow through the anchor region.

---

[3]2D-modes are modes with a two-dimensional displacement distribution, which can be observed in planar structures like plates or membranes.

We propose an alternative approach to the use of phononic crystals, which does not require constructive changes to the resonator or substrate by utilizing intrinsic properties of the system:

The anchor region of a plate resonator vibrating in a 2D plate-mode can be seen as a continuous distribution of point-sources of elastic energy. The mechanical waves which are emitted by these sources interfere with each other in the substrate. Depending on the distance between the individual sources, and their phase, this can lead to an increase or decrease of the total energy which is lost to the substrate. The mode order, and thus the number of nodal lines[4] corresponds to the number of sources of elastic energy, while the width of the resonator corresponds to the distance between the individual sources. The change in energy loss, and therefore the quality factor, should be especially significant when the distance between two sources is getting in the same order of magnitude as the dominating wavelength of the substrate wave field.

This approach is based on observations by Kähler et al [13], who described a similar effect in silicon micro-pillars. Figure 2 illustrates this analogy, where (a) shows the pillar resonators mentioned above, and (b) shows a plate resonator vibrating in its first torsional mode. The colors correspond to positive or negative displacement of the resonator in "vertical" direction. If this effect can be verified in plate resonators, it could possibly be utilized to control the quality factor for resonators dominated by anchor losses.

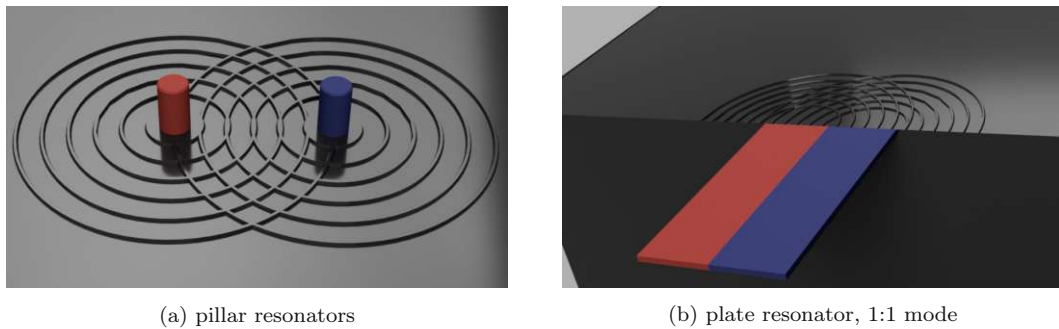(a) pillar resonators

(b) plate resonator, 1:1 mode

Figure 2: Analogy between two pillar resonators and a plate resonator vibrating in its first torsional mode.

Goal   In this work, we model plate resonators of various sizes numerically, with a focus on the behavior of anchor losses for 2D plate-modes. A major goal is to investigate how the local force distribution at the anchor effects the dissipation of energy to the substrate. We also expect a modulation of the quality factor with varying plate width for specific 2D plate-modes. In addition, we design an experiment to validate our numerical results.

---

[4]Nodal lines are zones with no displacement.

2. Anchor Losses

For vibrating microstructures in vacuum, a major source of loss are so-called anchor- or support losses, where elastic energy is radiated out through the intersection between the resonator and the substrate/chip, which is called the *anchor* . This mechanism is illustrated in Figure 3, where a plate resonator is attached to the edge of a substrate, which is large in comparison to the resonator dimensions. 3a shows the resonator vibrating in its first bending mode and 3b shows the first torsional mode. The color corresponds to the magnitude of total displacement. We can see, that the torsional mode causes a completely different displacement pattern in the substrate than the bending mode, forming two distinct side-lobes.

(a) fundamental bending mode

(b) fundamental torsional mode
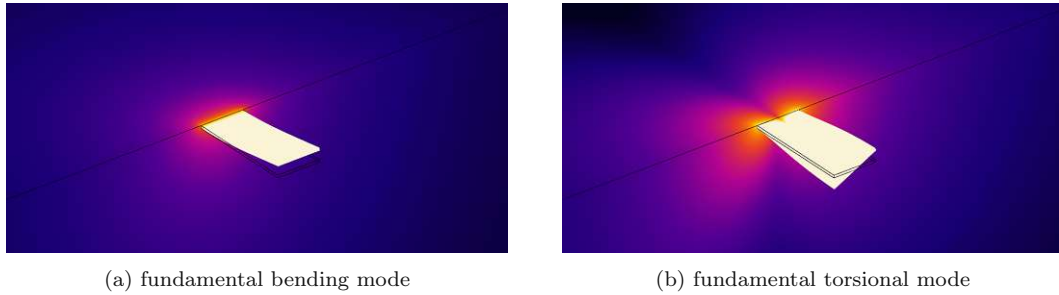
Figure 3: Magnitude of total displacement for the first bending- and the first torsional mode of a cantilevered plate resonator. The directional characteristic of the displacement is clearly visible. Colors are not to scale.

2.1. Analytical Models

There have been several attempts to derive analytical estimates for the quality factor of a beam shaped microstructure. These models have been proven to deliver estimates consistent with both numerical and experimental results for the fundamental flexural modes of isotropic, beam shaped resonators. There are no analytical models to predict the anchor-loss related quality factor for thin plates which are vibrating in higher order modes.

For an isotropic beam, attached to a semi-infinite substrate and vibrating in its first flexural mode, Judge et al. proposed the following analytical estimation for the quality factor [8]:

$$Q_{anchor}{}^{-1} = A \, \frac{w}{l} \left(\frac{t}{l} \right)^4 , \tag{5}$$

where the symbols l, w and t denote the length, width and thickness of the cantilever. The numerical coefficient A is a function of Poisson's ratio ν and is 0.29 for $\nu = 0.22$. It is important to note that different sized beams sharing the same aspect ratio, also have the same anchor-loss related quality factor.

This estimation agrees well with experiments for slender cantilevers attached to a

semi-infinite substrate (Figure 4a) [8]. However, it is not suited for geometries where the cantilever is attached on the top of a substrate chip as it is common for many applications like AFM cantilevers (Figure 4b).

(a) Beam attached to the substrate bulk.
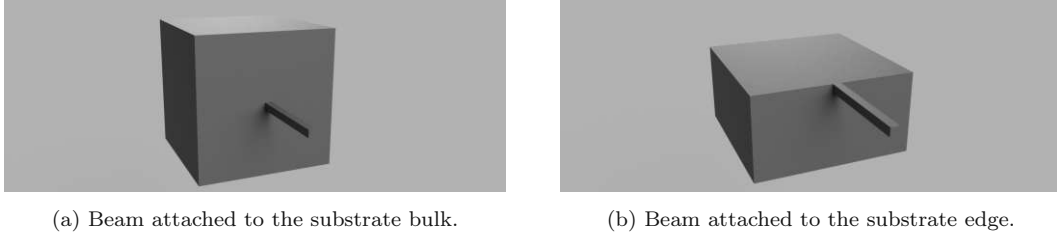

(b) Beam attached to the substrate edge.

Figure 4: Different cantilever placement on the substrate.

Another estimation has been derived by Wilson-Rae [9], which is based on the tunneling of phonons between the beam and the substrate. For out-of-plane bending modes, the quality factor can be approximated by

$$Q = \frac{3.9}{\pi^4 \, \delta \, C_n} \frac{l^5}{w \, t^4} \left(\frac{3\pi}{2 \, k_n \, l} \right)^4 , \tag{6}$$

where k_n are solutions of the equation $\cos(k_n l) \cosh(k_n l) = -1$. The parameter δ corresponds to the number of supports, e.g. 1 for a cantilevered beam, 2 for a bridge configuration. The constant C_n can be obtained as follows

$$C_n = \left(\tanh^2 \frac{k_n l}{2} \right)^{(-1)^{(n-1)}} . \tag{7}$$

This estimation is known to work well for isotropic beams with very high aspect ratios $(w/l \to 0)$, and can be generalized to longitudinal modes, as well as torsional modes of any mode order.

2.2. Numerical Approaches

While analytical methods often yield results close to reality for simple problems, they typically rely on a high level of simplification and do not generalize well to complex geometries. A commonly used numerical method to solve partial differential equations (PDEs) for arbitrary geometries is the finite element method (FEM) [14] [15], where the simulation space is subdivided into discrete smaller parts, the so-called finite elements. The finite elements are arranged in the *mesh* of the object, which represents a numerical domain of the solution. FEM is widely used in the scientific- and engineering space, as there are several commercial software frameworks available which wrap finite-element solvers in relatively easy to use CAD interfaces.

There are various examples in the literature [10] [11] where the anchor-loss related quality factor has been calculated for micromechanical devices using the finite-element method. A commonly used approach to conquer open domain problems is to embed a

finite substrate region into a so called perfectly matched layer (PML). This layer absorbs impinging elastic waves, using a complex coordinate transformation which can be seen as a form of impedance matching. The method was first developed by Berenger et al. [16], to solve open domain problems for the propagation of electromagnetic waves. The PML method is also suitable to investigate the propagation of elastic waves [17], and is therefore also used in our finite-element model, which is introduced in section 2.3.

Numerical studies by Frangi et al. [10] and Chen et al. [11] focus on the estimation of quality factors for the fundamental vibrational modes of slender and isotropic beams, and the validation of their results against well known analytical models like the ones by Judge (Eq. 5) or Wilson-Rae (Eq. 6). There are no studies on the behavior of the anchor-loss related quality factor of micromechanical resonators vibrating in non-fundamental modes of higher order.

2.3. Finite Element Model

To conduct the finite-element simulations, we use the FEM framework COMSOL Multiphysics 5.5. The devices of interest are plates with rectangular cross-section and are attached to a bulk substrate. The resonator and the substrate are both modeled as linear elastic material. To prevent the reflection of elastic waves on the edges of the substrate chip, a PML is placed around the substrate region. As sharp corners and edges on the substrate can impede the wave attenuating mechanism of the PML, the substrate is formed as a quarter of a sphere.

The substrate radius is set to two times λ_{SAW}, which is the expected wavelength of a surface acoustic wave, and is calculated by

$$\lambda_{\mathrm{SAW}} = \frac{v}{f_0}, \tag{8}$$

where v denotes the phase velocity (estimated 5092 m/s [13]) and f_0 is the natural frequency of the mode of interest. A substrate radius below two times λ_{SAW} leads to a worsened convergence of the solver. We will later use the top surface of the substrate as a "screen" to observe elastic wave propagation and possible interference patterns (see section 3.2). The PML thickness is set to at least λ_{SAW}, which will be addressed later in Section 2.3.1. Fluid damping should be ignored in this study and the surrounding environment is modeled as vacuum.
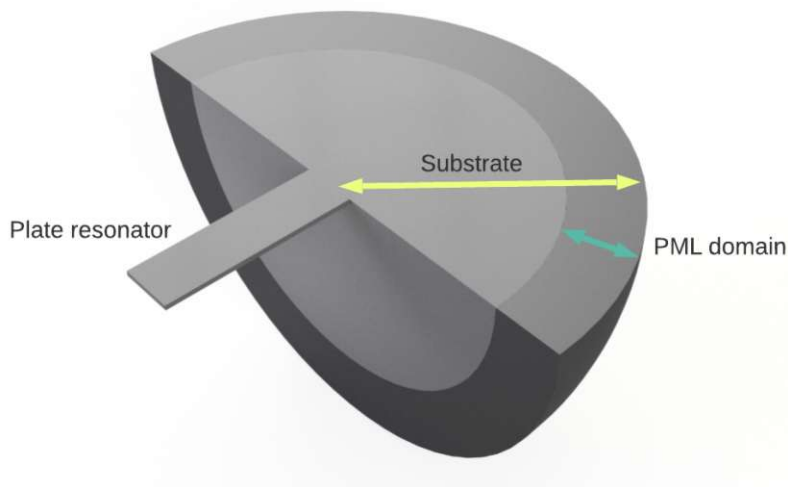
Figure 5: Rectangular cantilever attached to a quarter-spherical substrate with PML domain.

The mesh of the model can be seen in Figure 6. The cantilever top surface is meshed using free triangular elements, with a maximum element size of 2.5 % of the cantilever width. The top mesh is swept to the cantilever bottom, using a fixed number of three elements. The substrate is meshed using free tetrahedral elements, where the maximum element size is set to $\lambda_{\mathrm{SAW}}/2$. The quarter-spherical PML domain which is "coating" the substrate is meshed using a concentric swept-mesh. The number of elements in the PML is calculated by multiplying the parameters S_{PML} and M_{PML}, which are explained in Section 2.3.1.

To keep the model solvable in reasonable time on a local machine, it has been designed such that the degrees of freedom are not exceeding one million. When changing geometric parameters of the cantilever and the substrate, we checked that the average skewness[5] element quality indicator is not exceeding 0.25.

---

[5]Skewness indicates how close to equiangular a mesh cell is. Large skewness can compromise the accuracy of the interpolated domains. A equiangular mesh cell has a skewness of 0 which is therefore the optimal value.

(a) cantilever mesh

(b) complete mesh
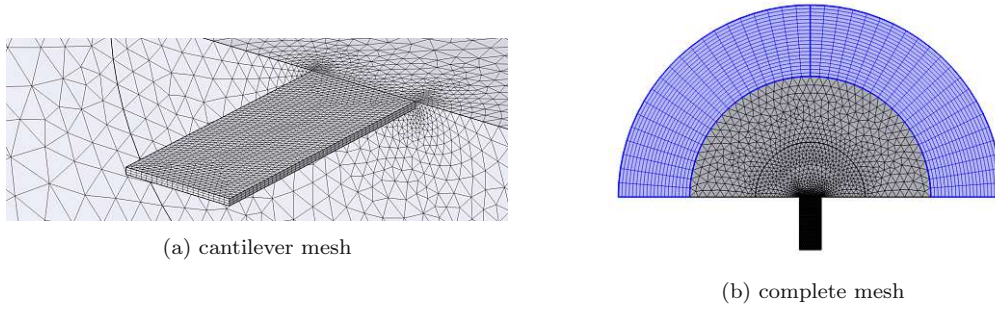
Figure 6: Meshing of the anchor-loss model. The cantilever top surface is meshed with free triangular elements, which are then swept over the cantilever thickness. The substrate is meshed using free tetrahedral elements. The PML (highlighted in blue) is meshed using a concentric swept-mesh.

To determine the natural frequencies and mode shapes of the system, a standard eigenfrequency analysis has been used. Since the substrate radius is dependent on the wavelength and thus on the frequency of vibration, the substrate radius has to be adapted for each mode of interest. This is done by running an eigenfrequency study on a smaller model, where the plate resonator without a substrate is set to a fixed constraint on one end. The wavelength λ_{SAW} can be calculated and the full model (including a substrate- and PML domain) is modified for the expected mode of interest.

In COMSOL, the quality factor is determined from the expression

$$Q = \frac{\mathrm{Re}(f_0)}{2\,\mathrm{Im}(f_0)},$$ (9)

where f_0 denotes the complex eigenfrequency which is determined numerically in an eigenmode analysis. Any damping in the system leads to a larger imaginary part in the eigenfrequency analysis. As the only source of damping in this system is the energy which gets dissipated in the PML, the quality factor is purely determined by anchor losses. It has been shown, that for systems that can be approximated by a 1D-spring-mass model, Eq. 9 gives very similar results as Eq. 1 [10].

2.3.1. PML Tuning and Model Stability

The mechanism of how the PML is absorbing impinging elastic waves can be tuned, using the following parameters[6]:

- The PML *thickness* T_{PML} is referring to the physical thickness of the PML shell. To ensure sufficient absorption, the PML should be at least as thick as the longest wavelength in the wave field.

- The *typical wavelength* λ_{typ} of the PML is the longest wavelength of propagating waves which are absorbed by the PML and is inversely proportional to the frequency. In our model, the typical wavelength is set to c/f_{sys}, where c is the phase velocity of the longest expected SAW wavelength. f_{sys} is the expected natural frequency of the mode of interest.

- The PML *scaling factor* S_{PML} is multiplied with the *typical wavelength* to improve the effective absorption for waves which are impinging at an angle θ relative to the PML boundary normal. This is necessary as the path length through the PML is increased for higher angles.

- The PML *curvature* C_{PML} can be used to remesh the PML domain. Increasing this parameter moves available mesh elements towards the substrate/PML boundary, and can be necessary when the wave field contains a mix of different wavelengths. As the elastic waves which are travelling through the substrate are expected to have a very narrow frequency range, which corresponds to the resonance frequency of the mode of interest, C_{PML} is set to one (1).

- The PML *mesh density* M_{PML} is a linear scaling parameter which increases the number of mesh elements in the PML domain.

The PML approximates an infinite substrate that absorbes all wave energy without significant reflection. To check the effectiveness of the PML implementation, we model a rectangular beam ($L \times W \times T = 125 \times 40 \times 6.25$ µm), which corresponds to the geometry of a Bruker AFM-Cantilever RTESPA-525[7]. The natural frequency of the first bending mode is 511 kHz and the anchor loss related quality factor is close to 400 000.

To monitor stability and convergence of the model, we perform sweeps of the parameters T_{PML}, S_{PML} and M_{PML} around their default values ($T_{\mathrm{PML}}^{(\mathrm{default})} = \lambda_{\mathrm{typ}}$, $S_{\mathrm{PML}}^{(\mathrm{default})} = 1$, $M_{\mathrm{PML}}^{(\mathrm{default})} = 12$), while keeping the other parameters constant. The dependency of the quality factors on the PML parameters are shown in the figures 7 to 9. The quality factor shows a very stable behavior close to and above the default values for all three parameters. The model becomes unstable for values of S_{PML} below 0.3 and values of T_{PML} below 8.

---

[6]https://doc.comsol.com/5.5/doc/com.comsol.help.comsol/COMSOL_ReferenceManual.pdf
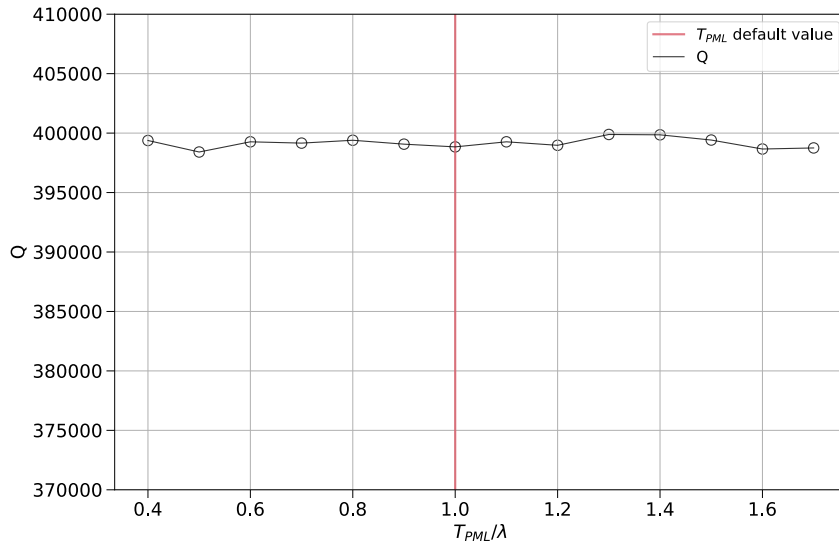[7]https://www.brukerafmprobes.com/p-3915-rtespa-525.aspx

Figure 7: Dependence of Q on T_{PML}, normalized to the longest expected wavelength. The red vertical line indicates the default value of T_{PML}.
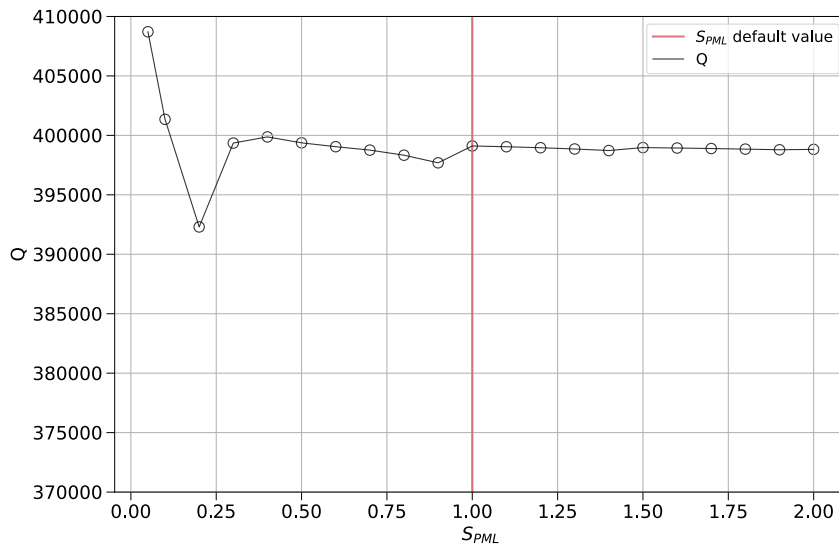

Figure 8: Dependence of Q on S_{PML}. The red vertical line indicates the default value of S_{PML}.
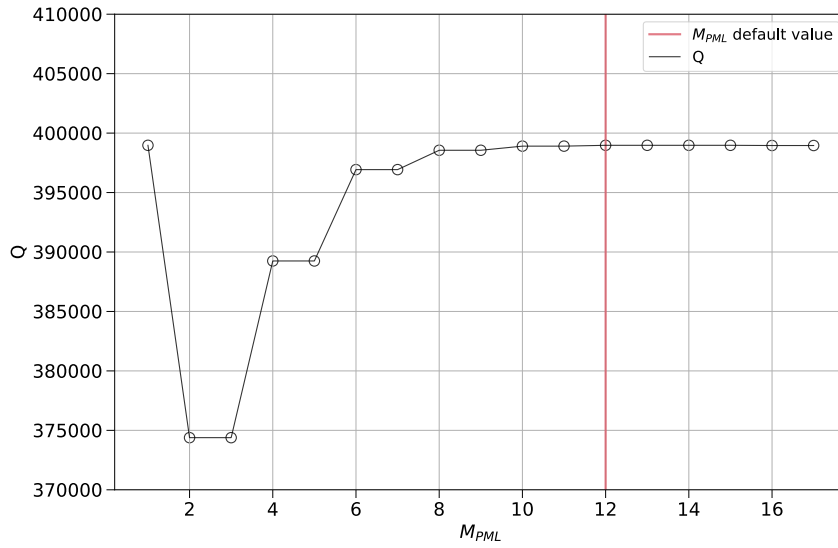
Figure 9: Dependence of Q on T_{PML}. The red vertical line indicates the default value of M_{PML}.

2.3.2. Model Validation

To validate our simulation results for the quality factor, we use the model by Judge et al (Eq. 5). As this estimation does not take into account any anisotropic effects or wafer orientation, we use polycrystalline silicon as material for our numerical simulations:

Density ρ	2320 kg/m^3
Young's Modulus E	169 GPa
Poisson's ratio ν	0.22

Table 1: Material properties of polycrystalline silicon.

As described in section 2.1, Judge's formula estimates the quality factor for a cantilever attached to a semi-infinite substrate. This case is represented by the model in Figure 10a, where the semi-infinite substrate is approximated by a hemispherical PML configuration. Resonators for sensing applications (e.g. atomic force microscopy) are often placed with their top surface flush with the substrate surface (Figure 10b). This configuration is used for most of the simulations in this work, but is expected to show less agreement with the analytical estimation by Judge.

11
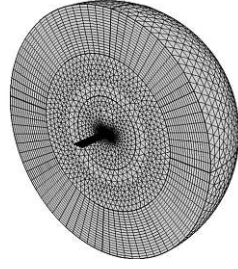
(a) cantilever attached to the center of a half-spherical substrate
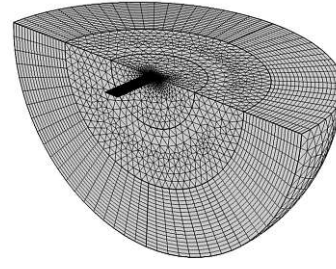
(b) cantilever attached to the edge of a quarter-spherical substrate

Figure 10: Different cantilever placement on the substrate. While (a) approximates a semi-infinite substrate, (b) approximates a cantilever attachment more similar to common real world applications like AFM cantilevers.

To validate the finite element model, the quality factor for the fundamental bending mode has been calculated for different cantilever geometries. The different resonator geometries cover different size regimes (L, M, S) and different aspect ratios (4 - long plate, 1 - square plate, 0.25 - wide plate). The dimensions of the M resonators are one fourth the dimensions of the L resonators, and the dimensions of the S resonators are again one fourth the dimensions of the M resonators.

Resonator	Length [µm]	Width [µm]	Thickness [µm]
L_4	800	200	10
L_1	400	400	10
$L_{0.25}$	200	800	10
M_4	200	50	2.5
M_1	100	100	2.5
$M_{0.25}$	50	200	2.5
S_4	50	12.5	0.625
S_1	25	25	0.625
$S_{0.25}$	12.5	50	0.625

Table 2: Different resonator geometries to validate the anchor loss model.

The validation results can be seen in Figure 11 and Table 3, respectively.
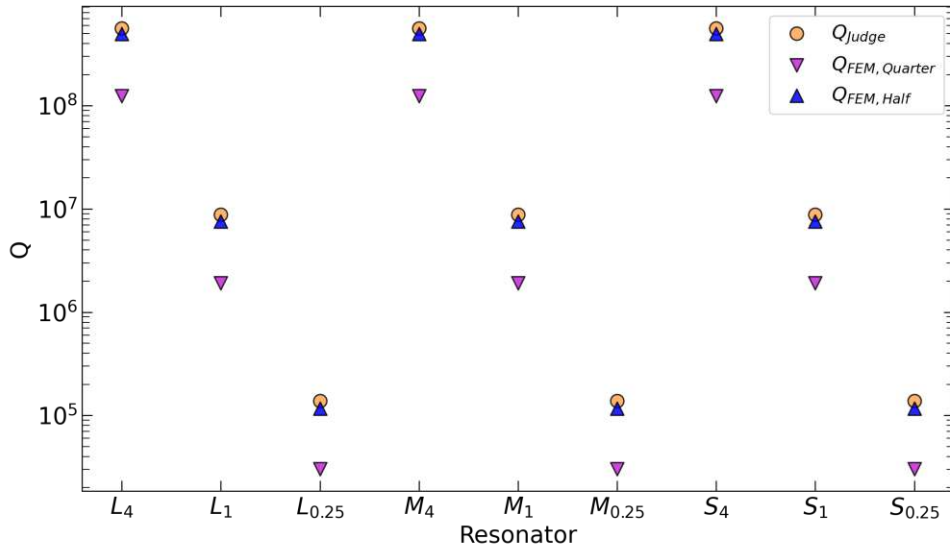
Figure 11: Model validation using Judge's formula. $Q_{FEM,Half}$ is referring to the configuration shown in Figure 10a, and $Q_{FEM,Quarter}$ is referring to the configuration shown in Figure 10b. The corresponding values for the quality factor can be seen in Table 3.

Resonator	f_0 [kHz]	Q_{Judge}	Q_{Half}	rel. diff. [%]	Q_{Quarter}	rel. diff. [%]
L_4	21.5	564 965 517	494 631 700	14.22	124 451 070	353.97
L_1	87.7	8 827 586	7 557 169	16.81	1 918 181	360.21
$L_{0.25}$	352.0	137 931	116 988	17.9	30 139	357.65
M_4	86.88	564 965 517	494 321 248	14.29	124 451 050	353.97
M_1	350	8 827 586	7 555 516	16.84	1 920 141	359.74
$M_{0.25}$	1 412	137 931	117 048	17.84	30 233	356.23
S_4	347	564 965 517	494 484 590	14.25	124 493 300	353.81
S_1	1 403	8 827 586	7 557 942	16.8	1 920 408	359.67
$S_{0.25}$	5 650	137 931	117 123	17.77	30 233	356.23

Table 3: Quality factors for nine different resonators. f_0 denotes the resonance frequency of the first bending mode. Q_{Quarter} and Q_{Half} are referring to the two configurations shown in Figure 10.

The configuration approximating a semi-infinite substrate shows a better agreement with the analytical estimation. Long, slender plates have higher quality factors than short, wide plates. As also notable in the analytic formula (Eq. 5), resonators with the same aspect ratio have also very similar quality factors. The good agreement between analytical model and numerical results validates the numerical model for a wide range of planar structures (plates and beams).

In Figure 12, we can see an illustration of the dependency of Q on geometric parameters

in Judge's estimation. Starting with a resonator geometry of $200 \times 200 \times 10$ µm, each parameter is varied over a certain range. The quality factor is increasing with rising resonator length, and decreasing with both rising width and thickness. The length of the plate has the greatest influence on the quality factor, followed by the thickness. This is also visible in Eq. 5, as the quality factor is proportional to l^5 and t^{-4}.
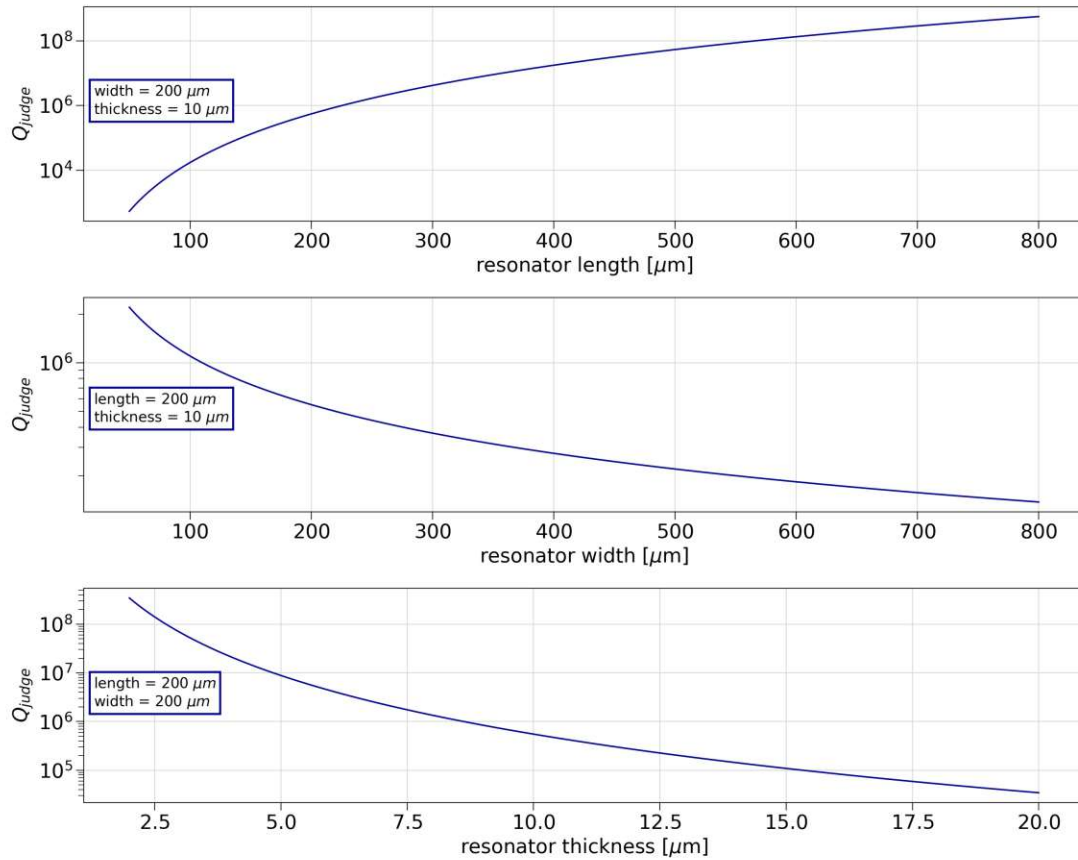
Figure 12: Quality factor estimation by Judge (Eq. 5), for a numerical sweep over length, width and thickness. Starting point is a $200 \times 200 \times 10$ µm plate resonator.

3. Vibrational Modes Beyond One Dimension

3.1. Vibrational Modes of Plates

The fundamental bending modes of long, slender beams can be described by the Euler-Bernoulli beam theory (see Appendix A.1), and the dynamics of such a beam can be approximated by a lumped-element model of the harmonic oscillator (see Appendix A.2).

As plate resonators have a higher number of spatial degrees of freedom than 1D-cantilevers, there is also a higher number of possibilities how mode shapes are formed. Figure 13 shows different mode shapes for a rectangular plate. A common convention is to distinguish different modes by their number of nodal lines perpendicular and parallel to the attachment point. The fundamental bending mode is identified by 1:0, the second bending mode by 2:0, the fundamental torsional mode by 1:1, and so on. This is known as Leissa nomenclature [18]. Not all modes can identified by this convention, as some modes do not have straight nodal lines and have therefore a more complex shape.

(a) 1:0   (b) 2:0   (c) 3:0

(d) 1:1   (e) 2:2   (f) complex shaped
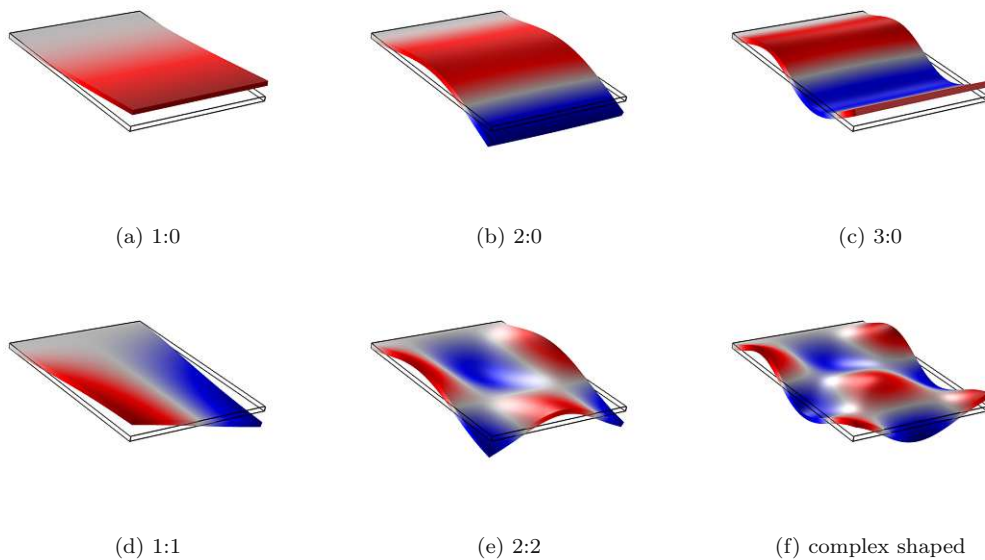
Figure 13: Displacement mode shapes for a thin, rectangular plate. Red indicates positive displacement and blue indicates negative displacement (in z-direction). The nodal lines (displacement = 0) can be used to distinguish the different modes. However, there are also more complex shaped modes, which can not be identified using this convention. Colors are not to scale.

A common problem when identifying different modes from their eigenmode shapes is *veering* [19]. When geometric parameters (e.g. width, length or thickness) of a resonator are changed, the frequency changes accordingly. As the rate of change is not necessarily the same for different modes, there might be some parameter values where the frequency curves are expected to cross. Close to this intersection point, the modes approach each

other in frequency, but just before crossing, they "repel each other" in frequency. During this process, the mode shapes are exchanged in a morphing process. The frequency curves do *not* cross, but the mode shapes are switched between the curves.

In this work, the individual modes are identified by their mode shape according to Leissa's nomenclature, which is a two-dimensional displacement distribution. As modes which show only a very small amount of veering are not easy distinguishable from modes with no veering at all, one has to pay special attention when selecting measurement or simulation data for post-processing. To avoid that this effect influences the quality factor, all data points which show significant veering have been removed from the datasets.
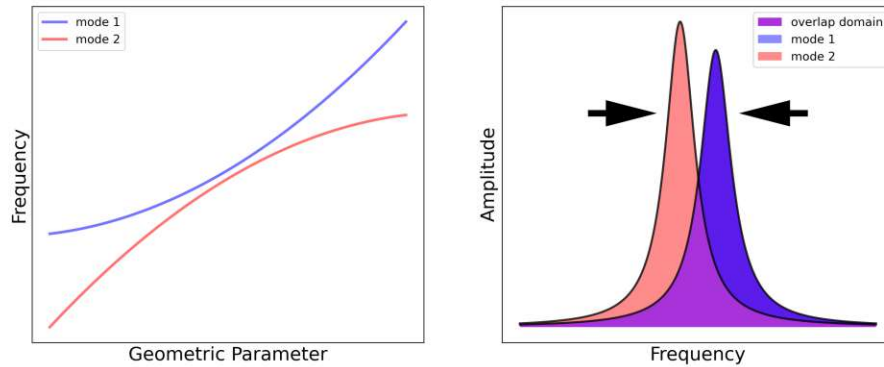
Figure 14: Illustration of veering. When two formerly distinct resonance peaks overlap each other, the modes cannot be easily separated anymore.

3.2. Directional Characteristics of Energy Transportation

In this section, we aim to get a qualitative understanding of the spatial distribution and directionality of the mechanical energy flux in the substrate. The quality factor of a resonator which is limited by anchor losses is inversely proportional to the total mechanical energy flux $\mathbf{I}_{\text{tot}}$ which is flowing through the anchor over one period of vibration.

To get the total mechanical energy flux, we calculate the surface integral of the normal mechanical energy flux over a quarter spherical surface (highlighted in blue in Figure 15):

$$I_{\text{tot}} = \iint_S I_i n_i \, dS, \tag{10}$$

where n_j denotes the normal vector to the integration surface. $\mathbf{I}$ is the local mechanical energy flux and is formed by the multiplication of the stress tensor σ and the velocity vector $\mathbf{v}$ [20]:

$$I_i = -\sigma_{ij} \cdot v_j \tag{11}$$
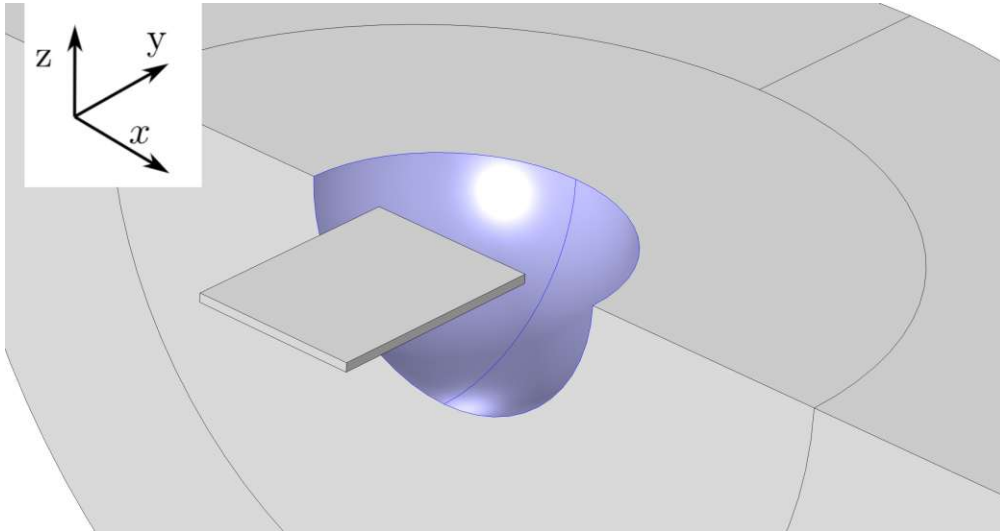
Figure 15: Illustration of quarter-spherical integration area, where energy leaves the anchor domain. The anchor region itself is hidden in this picture. All energy which is leaving the resonator has to pass through the blue-colored surface.

Figure 16 illustrates the inverse proportional relationship between the total energy flux and quality factor.
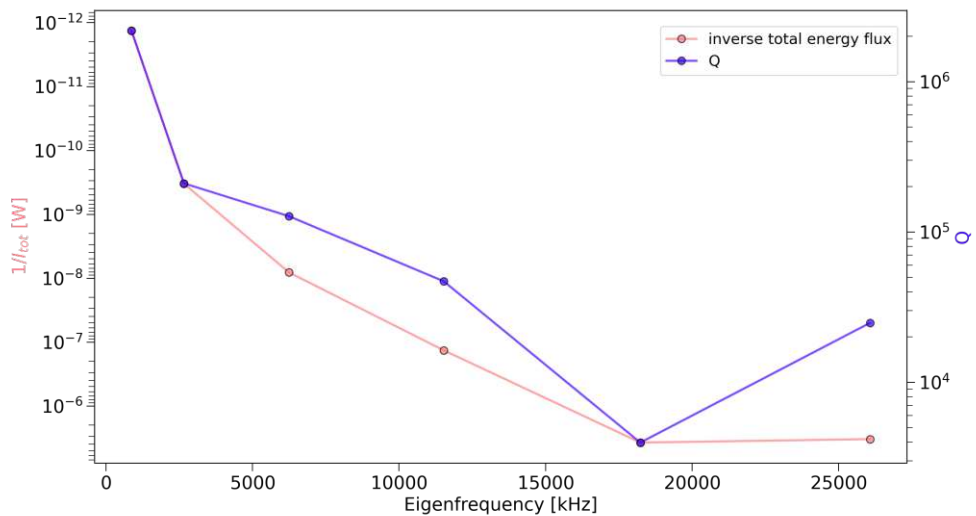
Figure 16: Inverse total net induced flux leaving the anchor region in comparison with the quality factor for six different modes of a plate resonator ($90 \times 90 \times 1.5$ µm). The data shown in this plot has been generated in a numerical study, using the model introduced in Section 2.3.

In the next step, we investigate the directional characteristics of the local mechanical

energy flux **I** for multiple 2D plate modes.

To keep things simple, we focus on modes with a single nodal line parallel to the anchor and multiple nodal lines perpendicular to the anchor (1:X in Leissa's nomenclature). These modes are commonly called roof tile-shaped modes, and the first six are illustrated in Figure 17.

(a) 1:2   (b) 1:3   (c) 1:4

(d) 1:5   (e) 1:6   (f) 1:7
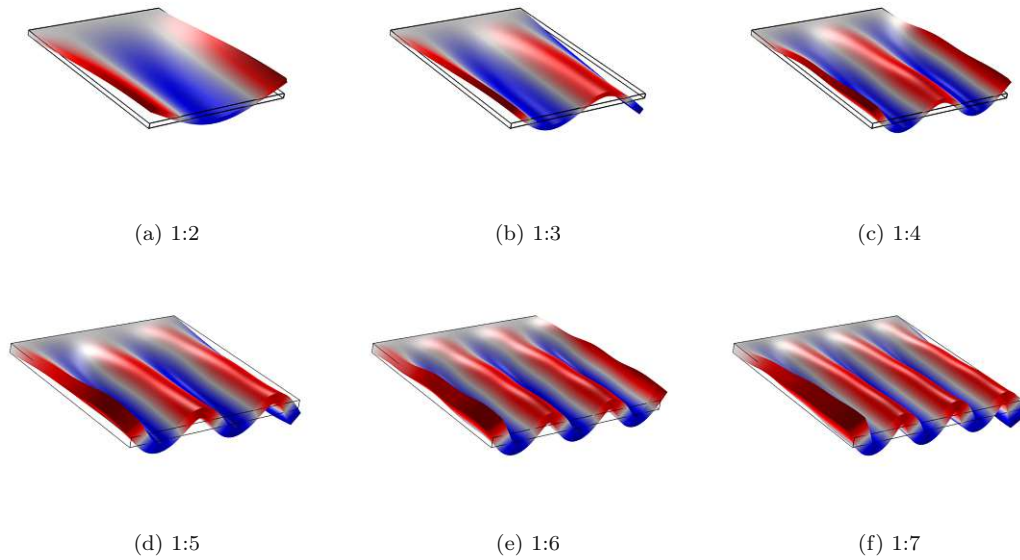
Figure 17: Roof tile-shaped modes shapes for a thin rectangular plate. Colors are not to scale.

To get a better understanding of the local effects of these kinds of modes, we look at the z-component of the displacement on the top surface of the substrate for the modes 1:0 to 1:7 (Figure 18).
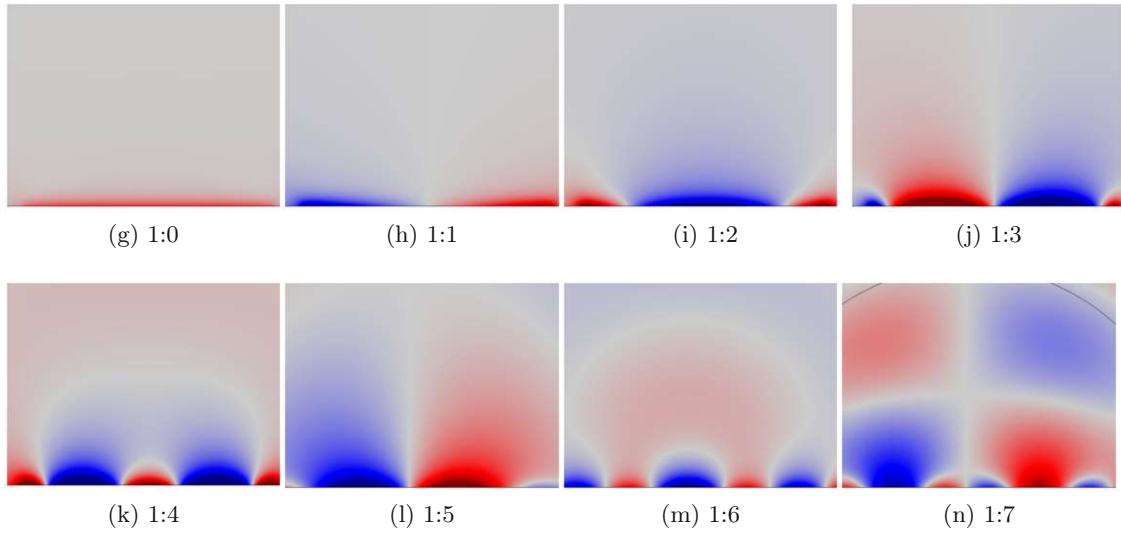
Figure 18: Z-component of displacement on the top surface of the substrate for different modes (1:0, 1:1, 1:2, 1:3, 1:4 1:5, 1:6, 1:7). The bottom of each plot represents the anchor point of the resonator. The resonator itself is not shown. Red indicates positive displacement, blue indicates negative displacement. Colors are not to scale.

The displacement field on the substrate surface exhibits a complex dependence on the x- and y-coordinates. The field is different for each mode, suggesting interactions between elastic energy waves from different "sources" in the anchor region. The mode order is therefore a parameter which directly influences the number of sources of elastic energy:

$$n_{\text{sources}} = n + 1, \tag{12}$$

where n is the number of nodal lines perpendicular to the anchor point. As these sources are interfering with each other, characteristic patterns are formed.

Figures 19 to 25 show the displacement magnitude and the normal mechanical energy flux, which is projected onto the inside of a semi-sphere ($r = \lambda_{\text{SAW}}$) that surrounds the anchor domain. As the resonance frequency increases with the mode order, the size of the substrate is decreasing in comparison to the size of the resonator. This is due to the dependence of the substrate radius on λ_{SAW}, which is again dependent on the resonance frequency (see Eq. 8). All colors are normalized for better visibility and therefore not to scale.
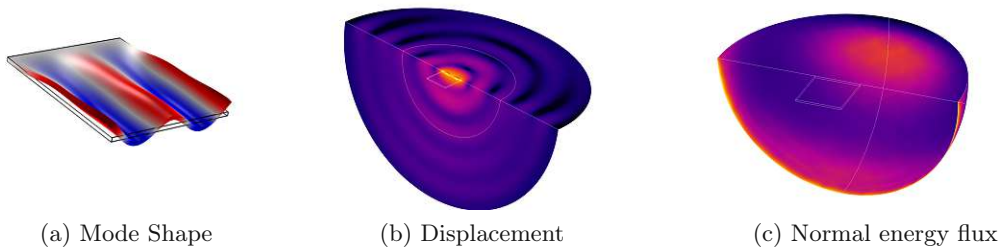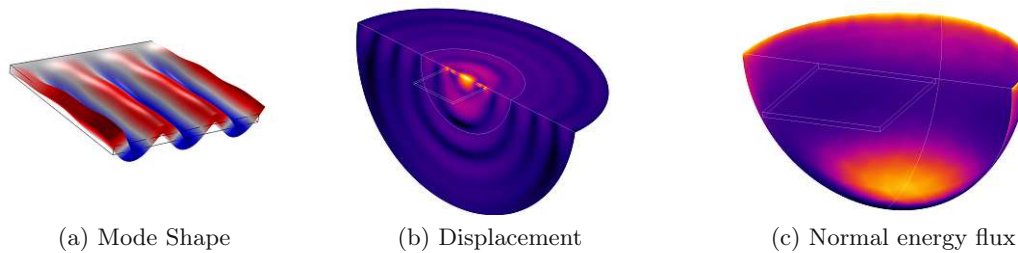
(a) Mode Shape   (b) Displacement   (c) Normal energy flux
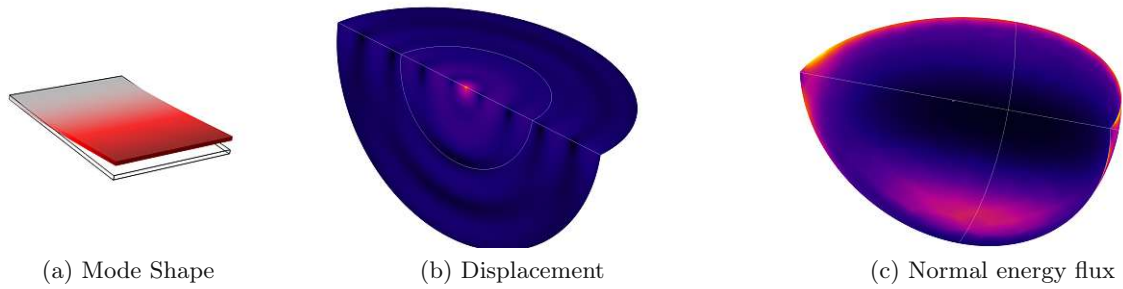
Figure 19: Displacement magnitude and normal mechanical energy flux for the 1:0 mode. Colors are not to scale.

For the fundamental bending mode (1:0), a large part of the energy leaves the anchor relatively evenly distributed in nearly all directions. Most of the energy is transported close to the surface. Additionally, there is a visible energy flux lobe pointing down in an angle of roughly 80° from the top surface.

(a) Mode Shape   (b) Displacement   (c) Normal energy flux
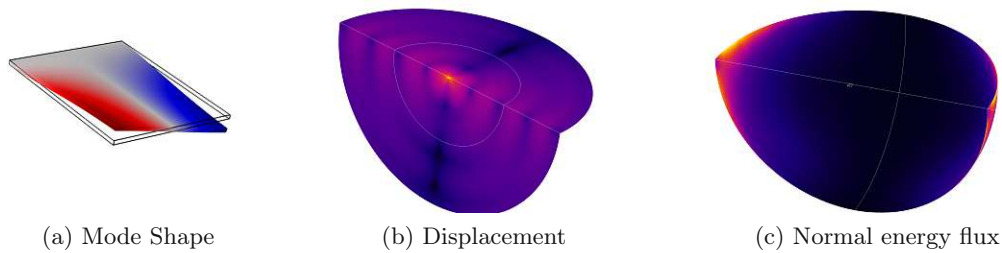
Figure 20: Displacement magnitude and normal mechanical energy flux for the 1:1 mode. Colors are not to scale.

When observing the displacement distribution of the 1:1 mode (Figure 20), we can clearly see two distinct sources of energy where the plate is attached to the substrate. In addition, the mechanical energy flux forms two very prominent side-lobes, and the energy flow appears to be smaller in positive y-direction.

(a) Mode Shape (b) Displacement (c) Normal energy flux
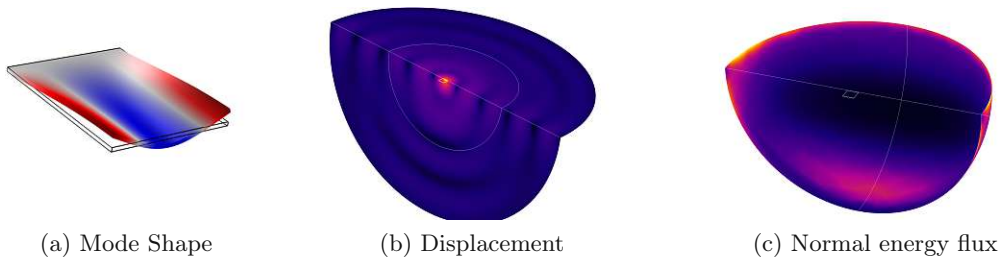
Figure 21: Displacement magnitude and normal mechanical energy flux for the 1:2 mode. Colors are not to scale.

The 1:2 mode in Figure 21 shows a very similar behavior to the 1:0 mode in Figure 19.

(a) Mode Shape (b) Displacement (c) Normal energy flux
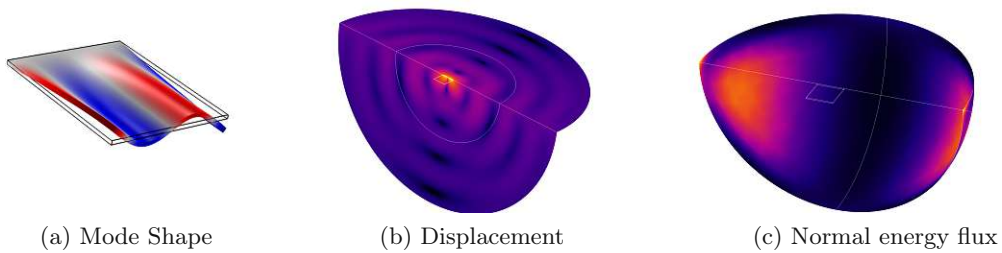
Figure 22: Displacement magnitude and normal mechanical energy flux for the 1:3 mode. Colors are not to scale.

The 1:3 mode in Figure 22 shows a very similar behavior to the 1:1 mode in Figure 20, and we can again see two very prominent side lobes of the mechanical energy flux. This could indicate a possible dependency between the energy flux distribution and the mode order, as both modes feature an odd number of nodal lines in their mode shape.

(a) Mode Shape (b) Displacement (c) Normal energy flux

Figure 23: Displacement magnitude and normal mechanical energy flux for the 1:4 mode. Colors are not to scale.

For the 1:4 mode in Figure 23, we can see that the majority of the energy flux is split in two directions. One major part is emitted in a frontal lobe (pos. y-direction) into

21

the substrate at roughly 20° from the top surface. The other major part is travelling downwards, close to the front surface.

(a) Mode Shape 　　　　　 (b) Displacement 　　　　　 (c) Normal energy flux
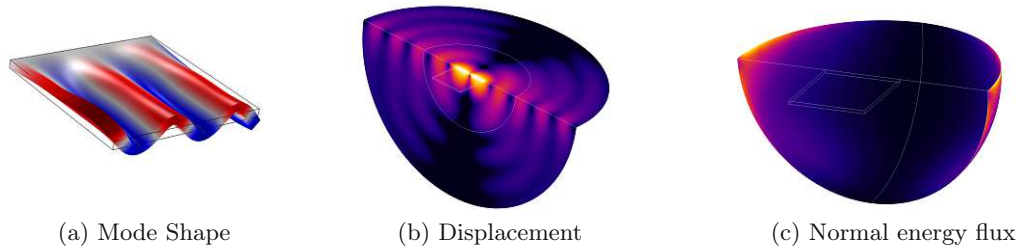
Figure 24: Displacement magnitude and normal mechanical energy flux for the 1:5 mode. Colors are not to scale.

The 1:5 mode shows again a very similar behavior as the modes 1:1 and 1:3, which reinforces our hypothesis that modes with an odd number of nodal lines in their mode shape feature a similar behavior in their distribution of the mechanical energy flux.

(a) Mode Shape 　　　　　 (b) Displacement 　　　　　 (c) Normal energy flux

Figure 25: Displacement magnitude and normal mechanical energy flux for the 1:6 mode. Colors are not to scale.

The normal mechanical energy flux of the 1:6 mode looks similar as the 1:2 mode and shows a inverted pattern as the 1:4 mode. One part of the energy is transported close to the top surface, and evenly distributed in all directions. The other part is emitted in a fairly concentrated lobe downwards, in an angle of roughly 20° from the front surface.

In conclusion, all modes featuring an odd number of nodal lines (1:1, 1:3, 1:5) show a similar behavior regarding the mechanical energy flux, which is divided into two distinct lobes. The energy flux in forward (positive y) direction is attenuated for these kinds of modes. The modes with an even number of nodal lines (1:0, 1:2, 1:4, 1:6), show also a very similar behavior, where the energy flux is split into two distinct parts. One part is travelling along one of the surfaces, the other part is concentrated in a lobe into the substrate.

As surface acoustic waves play a major role in various sensing applications, we try to get a more quantitative understanding of the mechanical energy flux close to the surface.

We do this by using the top surface of the substrate as a "screen", on which we can analyze the energy flow on the top surface of the substrate. This is illustrated in Figure 26, where the observation zone is highlighted in blue.
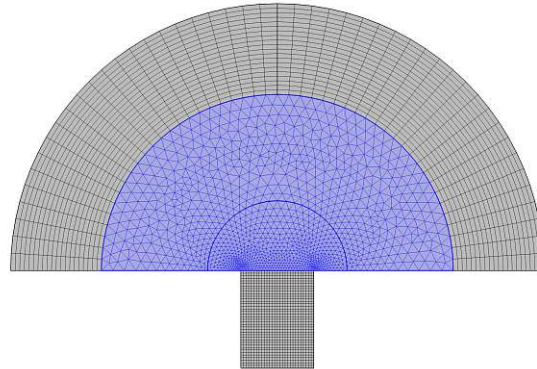
Figure 26: View of the top-surface of the resonator. We use the highlighted area as a "screen" to observe the behavior of the mechanical energy flux on the surface. The simulation results can be seen in figures 27 to 34.

The following figures (27 - 34) show the mechanical energy flux on the top surface for the modes 1:0 to 1:7, as well as the normal mechanical energy flux, which is leaving the anchor region through circles with different radii. By calculating the projected normal energy flux through these circles, the directional characteristic of the mechanical energy flux can be analyzed for different distances from the anchor. Due to the fact that the size of the substrate is dependent on the expected wavelength, the substrate is again smaller for higher frequencies.
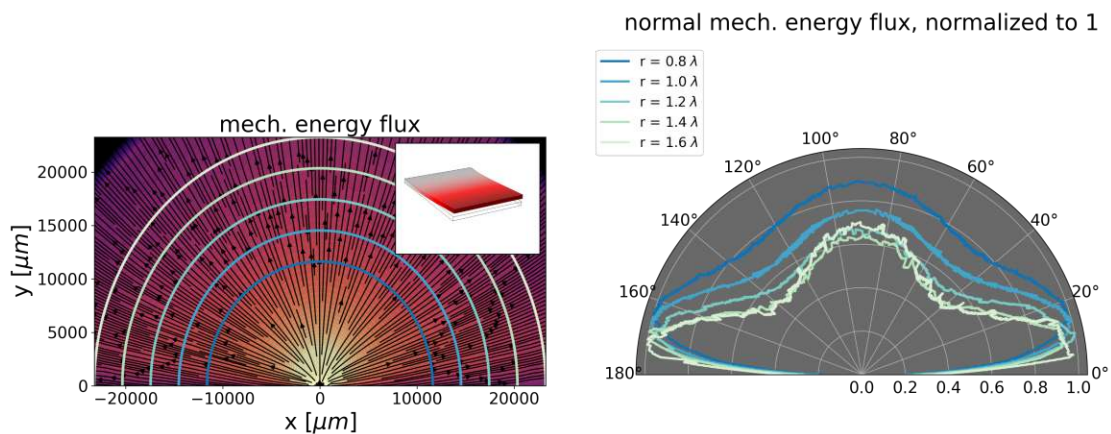
Figure 27: Mechanical energy flux for the 1:0 fundamental bending mode. The energy flux normal to the circles can be seen in the right plot (normalized 0-1).

For the 1:0 mode, we can see that most of the energy is radiated uniformly in forward

direction (20-160°), at least close to the anchor. With increasing distance, significant side-lobes are forming at angles of 10-20° and 160-170°.
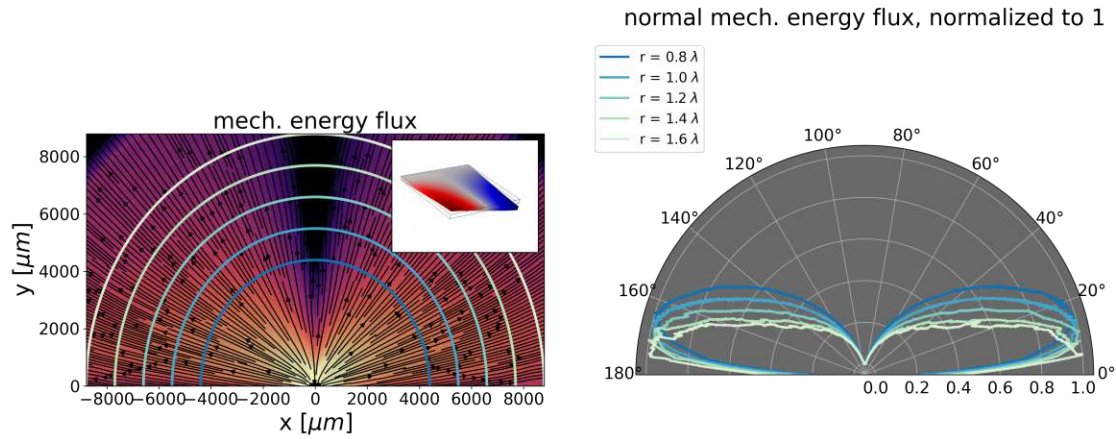
Figure 28: Mechanical energy flux for the 1:1 torsional mode.

For the 1:1 mode, most of the energy is radiated in the form of two side-lobes below 30 °. The energy flux in forward direction is nearly completely blocked, which leads to a very prominent "dark field" in 90 ° direction. This is also visible in the 3D plots in Figure 20.
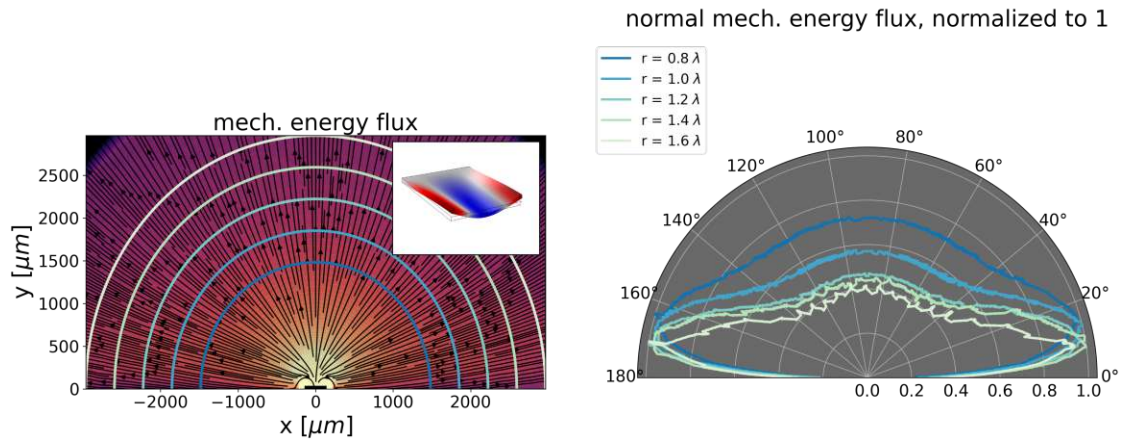
Figure 29: Mechanical energy flux for the 1:2 roof tile-shaped mode.

The 1:2 mode shows a very similar pattern to the 1:0 bending mode. A possible explanation for the similarity could be that both modes exhibit a single, relatively large elastic energy "source" at the center of the anchor region. For the 1:2 mode, the two additional sources on the side of the plate (marked in red in Figure 29) seem to contribute less to the overall energy flux in comparison to the central source (marked in blue). This is also visible in Figure 18i.

24
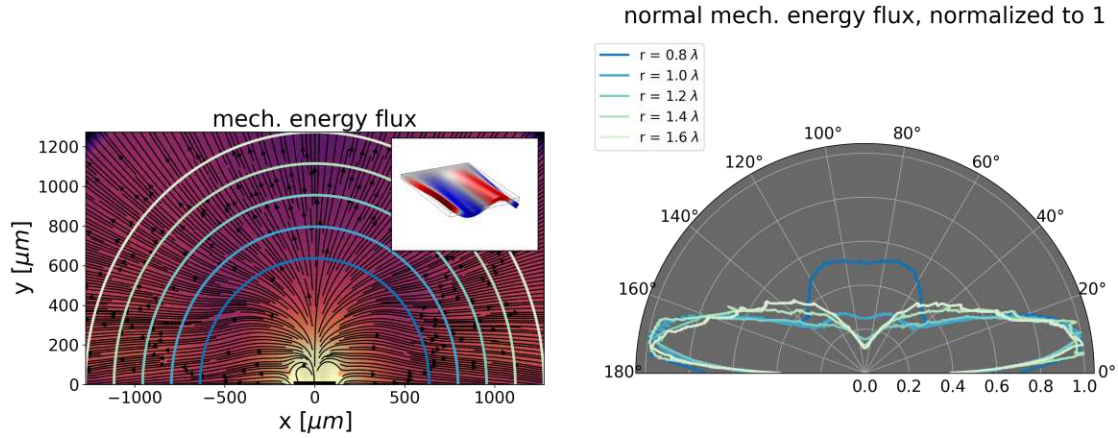
Figure 30: Mechanical energy flux for the 1:3 roof tile-shaped mode.

For a radius greater than one SAW-wavelength, the pattern of the 1:3 mode looks similar to the 1:1 torsional mode. Below one SAW-wavelength, a characteristic front-lobe is forming in 70-110° direction.
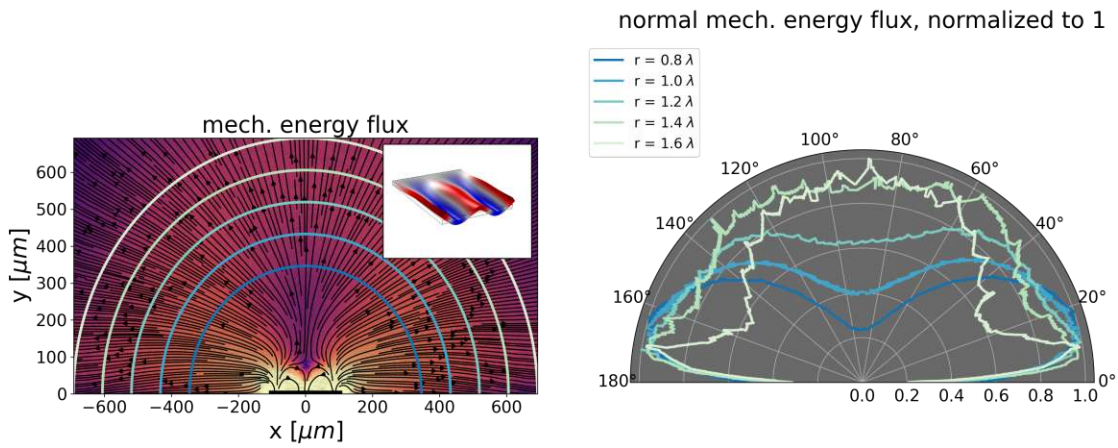
Figure 31: Mechanical energy flux for the 1:4 roof tile-shaped mode.

The 1:4 mode shows an opposite behavior as the 1:3 mode. For distances close to the anchor, the characteristic side lobes are present, while for higher distances a higher amount of energy is also emitted in forward direction (50-110°). The alternating pattern is likely due to a coarser mesh density at the edge of the geometry, and therefore a numerical artifact.
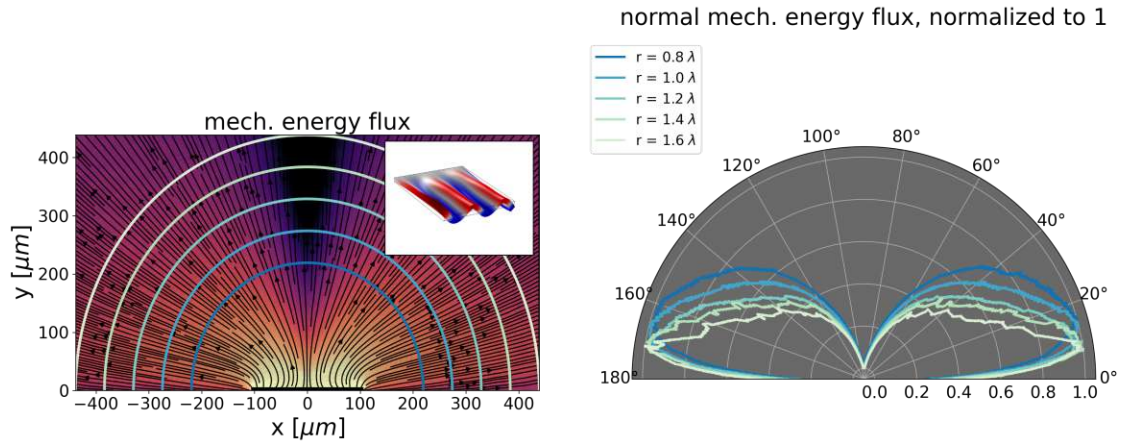
Figure 32: Mechanical energy flux for the 1:5 roof tile-shaped mode.

The 1:5 mode shows again a very similar behavior to the 1:1 torsional mode. For higher distances from the anchor, it also behaves similar to the 1:3 mode.
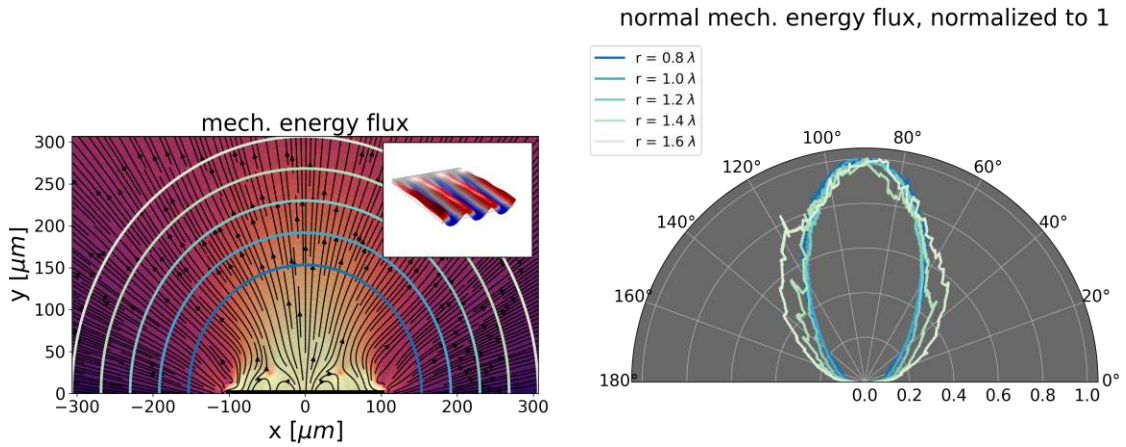
Figure 33: Mechanical energy flux for the 1:6 roof tile-shaped mode.

For the 1:6 mode, the majority of the energy radiated in forward direction, forming a central lobe between 50 and 130 °.
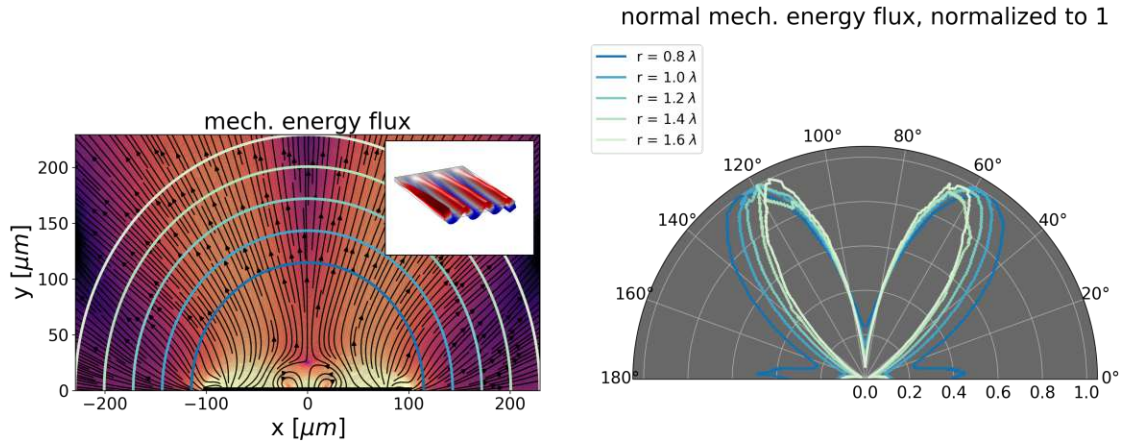
Figure 34: Mechanical energy flux for the 1:7 roof tile-shaped mode.

The 1:7 mode has a similar behavior than the other antisymmetric modes, but the side lobes are elevated to a higher angle of about 60 and 120 °.

In conclusion, the energy flux of the antisymmetric modes (1:1, 1:3, 1:5, 1:7) forms characteristic side lobes on the top surface, where most energy is radiated in two symmetric directions. For these modes, the energy emitted in frontal direction is relatively low. Symmetric modes (1:0, 1:2, 1:4, 1:6) show a more evenly distributed pattern which specific form is highly dependent on the distance from the anchor. This very distinct behavior of the energy flux of symmetric and antisymmetric modes can also be observed in the 3D representation (see figures 19 to 25). For the 1:6 mode, the energy flux on the top surface behaves different to all other modes, as it radiates most energy in a concentrated frontal lobe.

3.3. Anchor Loss Modulation for 2D-Modes

As we have stated in the introduction (see Section 1), we now want to examine if the anchor-loss related quality factor shows modulations dependent on the width of the plate (and therefore the separation distance of the sources of elastic energy). The following figures show simulation results for the FEM model introduced in Section 2.3, where the quality factor is dependent on the width of the plate.

Different vibrational modes are compared for a $(90 \times 50 - 300 \times 1.5 \ \mu m)$ plate resonator. First, we have a look at the behavior of flexural bending modes, which are presented in Figure 35.
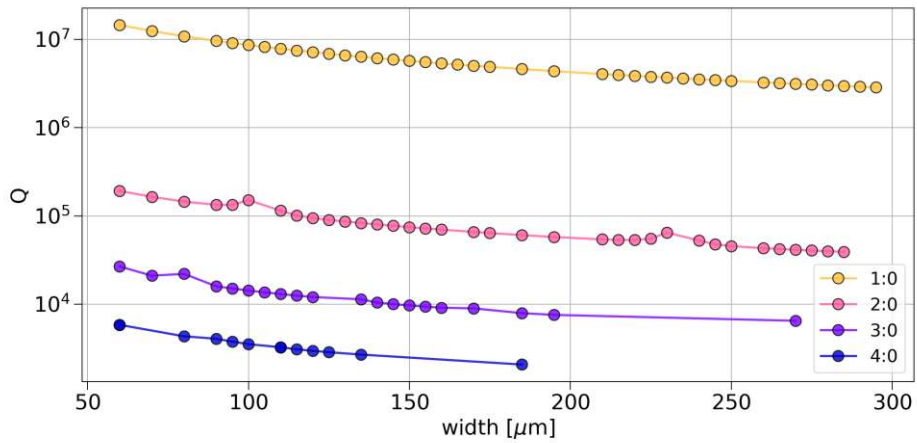
Figure 35: Quality factor dependent on cantilever width for flexural bending modes of a $90 \times 50 - 300 \times 1.5$ µm plate resonator.

The first four flexural bending modes show a declining trend for the quality factor with increasing plate-width. No oscillations are visible, which is plausible as bending modes have no nodal lines perpendicular to the anchor, so there is just a single "source" emitting energy to the substrate. Figure 36 shows the first three torsional modes, which have a single central nodal line along the cantilever and perpendicular to the anchor:
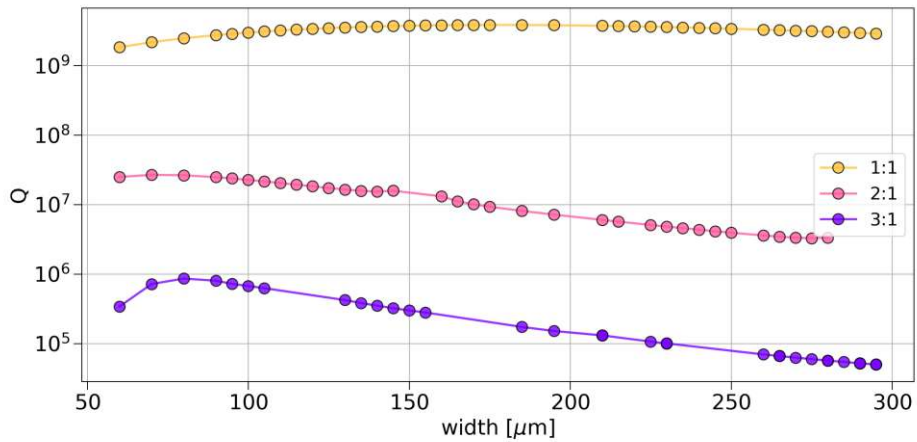
Figure 36: Quality factor dependent on cantilever width for torsional modes of a $90 \times 50 - 300 \times 1.5$ µm plate resonator.

We see a similar pattern as for the bending modes, with the only difference for the 3:1 mode, which has a maximum in the Q factor at about 70 µm before it decreases similarly as the previous modes, with a decline rate of about 10^{-5600x}.

In Figure 18, we have shown that the number of sources of elastic energy is directly tied

28

to the number of nodal lines touching the anchor. As interference effects are expected to influence the quality factor for an increasing number of sources, it would make sense to investigate modes with a higher number of nodal lines touching the anchor. To keep things simple, we will again focus on roof tile-shaped modes.

Figure 37 shows the width dependent quality factor for the roof tile-shaped modes 1:3 to 1:6.
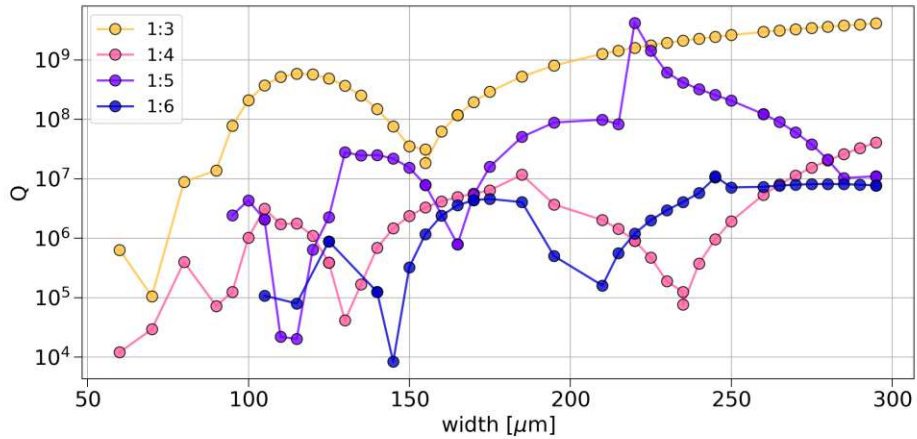
Figure 37: Quality factor dependent on cantilever width for roof tile-shaped modes of a 90x50-300x1.5 µm plate resonator.

For this selection of modes, we see an alternating pattern where the quality factor is oscillating over several order of magnitudes. A rising number of "sources" (which corresponds to the number of nodal lines touching the anchor) increases the total number of maxima and minima of the Q-factor. This is a significant difference to the behavior of the quality factor for bending- and torsional modes.

We will now have a deeper look at the width-dependent quality factor of roof tile-shaped modes. Figure 38 shows the quality factor dependent on cantilever width for a plate resonator (L = 90 µm, T = 1.5 µm), for the modes 1:1 to 1:6. The width is again altered from 50 to 300 µm.
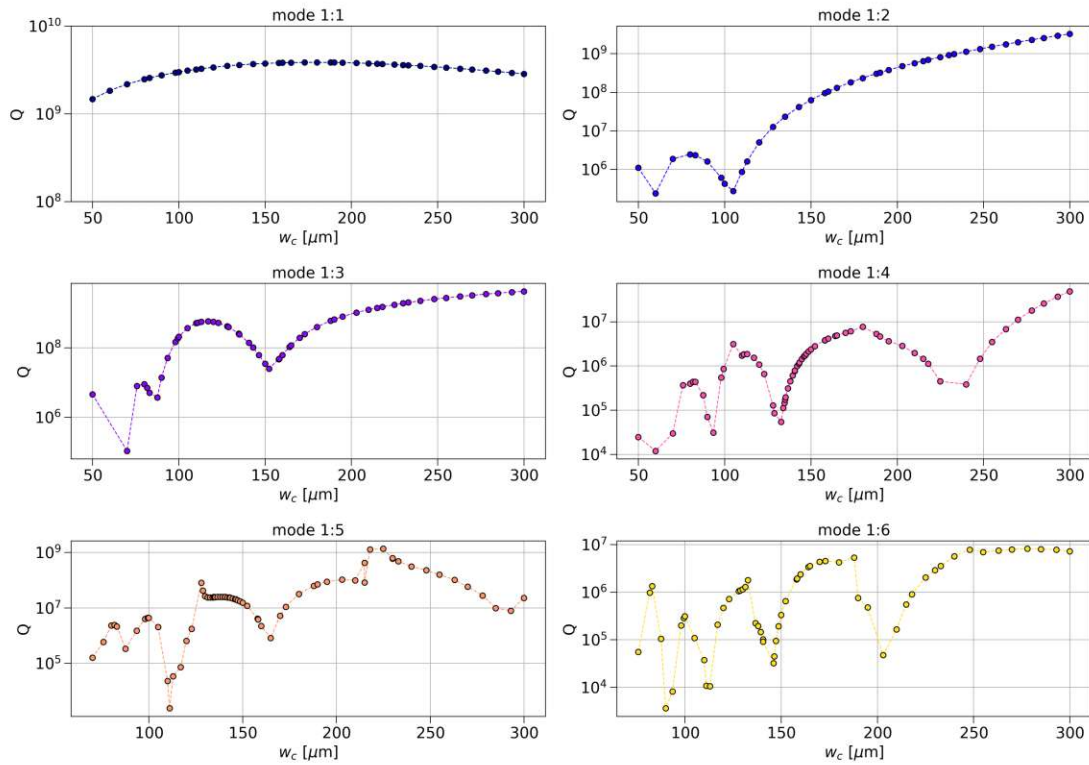
Figure 38: Quality factor dependent on cantilever width for a plate resonator (L = 90 µm, T = 1.5 µm), for the modes 1:1 to 1:6.

The quality factor shows oscillations spanning over several order of magnitude in amplitude, with a general trend to higher quality factors with increasing plate width. The number of oscillations is clearly related to the mode order and thus to the number of nodal lines which correspond to the number of elastic energy sources.

To get a better understanding of this effect, Figure 39 shows the same data, but the width is normalized by the estimated SAW wavelength in the substrate λ_{SAW}.
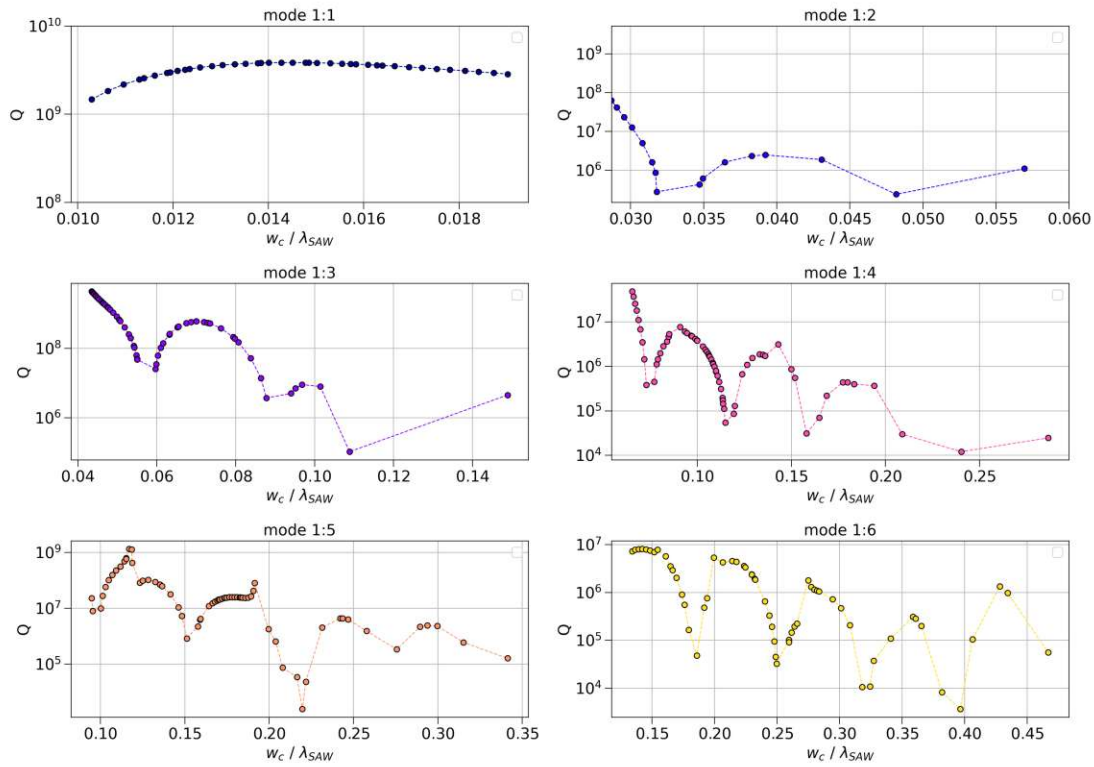
Figure 39: Quality factor dependent on cantilever width normalized to wavelength for a plate resonator (L = 90 µm, T = 1.5 µm), for the modes 1:1 to 1:6.

We see that the period length of the oscillations in the quality factor decreases for higher mode orders, while the ratio between plate width and substrate wavelength approach in the same order of magnitude. This phenomenon is especially visible when comparing the 1:6 mode to the modes 1:2 and 1:4. A similar behavior for different modes indicates that the same mechanism is present for all modes.

The alternating pattern also reinforces our hypothesis (see Section 1) that interference effects in the substrate could possibly be utilized to gain control over the quality factor, and therefore the performance characteristics of a resonator dominated by anchor losses. As a next step, we will try to validate our findings experimentally. The process of designing a suitable resonator and experimental validation of the simulation results is presented in the following sections.

4. Device Design and Fabrication

In Section 3.3, we have shown that the quality factor of specific 2D modes of plate resonators is modulated by an oscillating pattern, dependent on the width of the plate. In the following section, we describe the design process of a resonator to validate the numerical anchor loss modulation results experimentally.

31

4.1. Thermoelastic Limit for Experiment Design

Thermoelastic damping (TED) is also a significant loss mechanism that needs to be taken into account. In this work, TED is mostly investigated for the reason of later experiment design, as it can inflict a limit on the measurability of the anchor loss related quality factor. The reason is that the total quality factor of a system is calculated by adding up the reciprocal quality factors of the individual loss mechanisms. In our simulations, we assume, that the only loss mechanisms are anchor losses and TED, which simplifies Eq. 4 to:

$$\frac{1}{Q_{\text{tot}}} = \frac{1}{Q_{\text{anchor}}} + \frac{1}{Q_{\text{TED}}} \tag{13}$$

When thermoelastic losses dominate, changes in Q_{anchor} are harder to see. For this reason, it is crucial that Q_{anchor} is lower, or at least not higher by orders of magnitude, than Q_{TED}.

The following pages cover the design and validation of the finite element model for thermoelastic damping. In contrast to the model for anchor loss simulations, the model for thermoelastic damping does not comprise a substrate or PML. The cantilever is fixed on one end, and at this intersection, the temperature is set to room temperature. This ensures that generated heat can leave the cantilever domain at the attachment point. The remaining surfaces of the cantilever are modeled as thermal insulators, which emulates the effect of vacuum and assumes no heat radiation. To simulate the effect of thermoelastic damping, the *Solid Mechanics* module has been coupled with the *Heat Transfer in Solids* module, using the multiphysics interface.

To validate the thermoelastic model, the same resonator geometries as in Table 2 have been studied. The resonator material is again polycrystalline silicon, and the ambient temperature is set to room temperature. The quality factors of the mechanical modes have been calculated using the previously introduced finite element model, and are being compared to the analytical estimation by Roszhart [36].

The results are presented in Table 4 and Figure 40. As we can see, smaller resonators feature higher quality factors for the same aspect ratio. When comparing cantilevers in the same size domain, the quality factor is higher for long, slender plates than for short but wide plates. Interestingly, the relative error is generally small, but higher for long, slender beams. This is unexpected, as Roszhart's estimation has been derived exclusively for slender geometries.

Table 4: Quality factors for thermoelastic damping in comparison with analytical estimation by Roszhart.

Resonator	$f_0\,[kHz]$	Q_{Roszhart}	Q_{FEM}	rel. diff. [%]
L1	20.9	78657	122251	35.66
L2	83.8	20487	25459	19.53
L3	347.4	9928	7520	32.02
M1	83.2	310279	488412	36.47
M2	344.7	77320	99622	22.39
M3	1382.8	20375	22626	9.94
S1	344.3	1242680	1950662	36.29
S2	1378.9	307423	397996	22.76
S3	5531.4	76641	88718	13.61
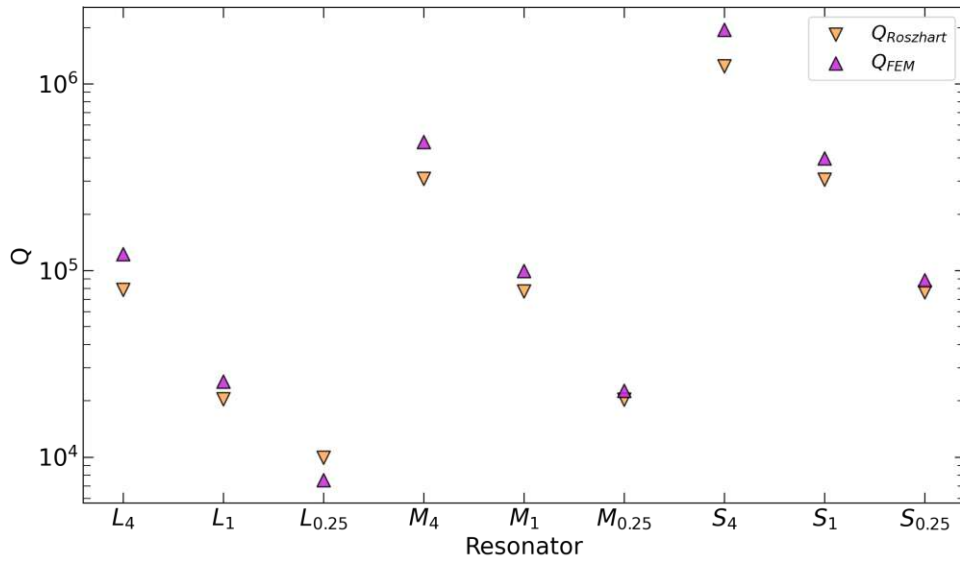
Figure 40: TED model validation using Roszhart's formula 36. The ambient temperature is set to 293.15 K.

4.2. Resonator Design Process

There are two major limitations which have to be considered when designing the devices for experiments:

1. The specifications and limitations of the measurement setup, especially the maximum measureable frequency.

2. The limit, at which the thermoelastic losses dominate over the anchor losses.

To determine the quality factor, we use a laser-doppler vibrometer (LDV) in combination with a lock-in amplifier (see section 5.1 for details). The highest measurable frequency

33

of vibration of the LDV is 24 MHz[8], so the maximum frequency for the highest mode of interest must be below that threshold. In addition, Q_{anchor} should be smaller than Q_{TED}, such that the measured total quality factor Q_{tot} is dominated by anchor losses.

Figure 41 shows FEM simulation results of quality factors for the 1:6 mode of a plate resonator out of polycrystalline silicon with the following dimensions: L × W × H = $90 \times 90 - 300 \times 1.5$ µm. The resonance frequencies for this plate are well below the maximum frequency of the measurement setup, but the quality factor is dominated by thermoelastic damping.
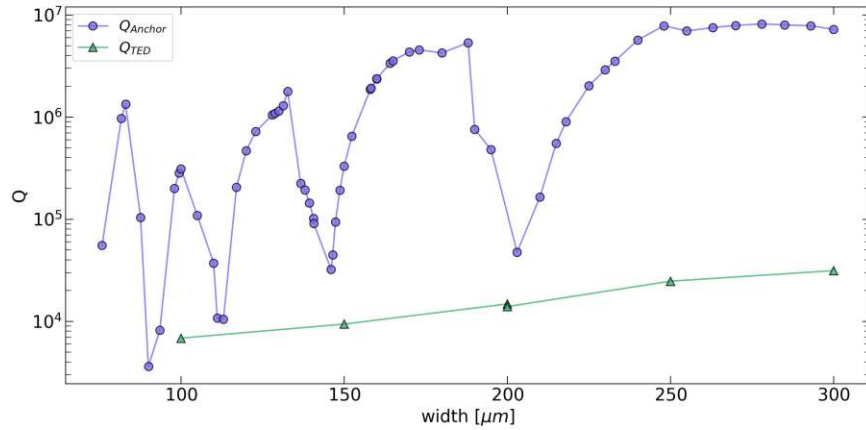
Figure 41: Quality factors for the 1:6 mode of a rectangular plate (L × W × H = 90 × $90 - 300 \times 1.5$ µm). Q_{TED} is clearly dominating the total quality factor.

The analytical estimation by Roszhart (see Appendix A.4) suggests that the choice of the thickness of the plate has a major impact on Q_{TED}. Figure 42, shows Q_{TED} as a function of plate thickness. As it can be observed, an increase in plate thickness can either increase or decrease the quality factor for a specific mode of interest. This is due to the frequency dependence of the thermoelastic damping.

---

[8]The frequency limit of 24 MHz is set by the DD-300 displacement decoder, which is a part of the MSA-500 LDV.
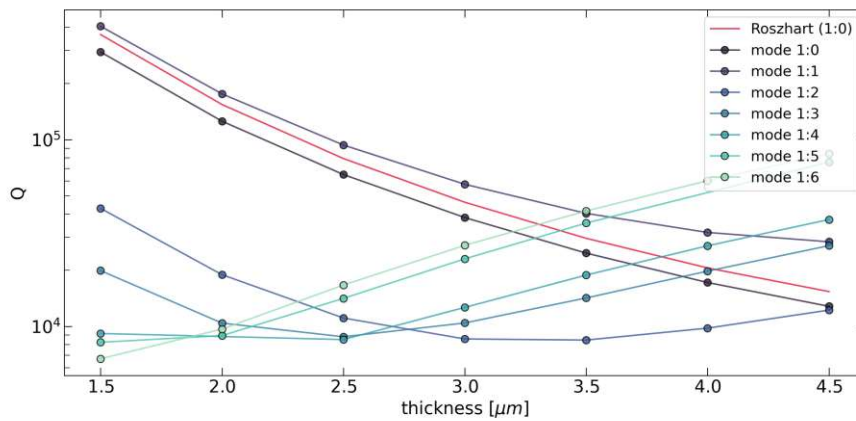
Figure 42: Q_{TED} as a function plate thickness for different modes. The red line shows the analytical estimation by Roszhart for the 1:0 mode for comparison.

As we are especially interested in roof tile-shaped modes of higher mode order, the model suggests increasing the plate thickness to increase the quality factor associated to thermoelastic effects. In Figure 42 we see, that for the 1:6 mode, Q_{TED} shows an increasing trend with higher plate thickness. At 4.5 µm, Q_{TED} is below 10^5. This is still low, when comparing this value to the anchor-loss related quality factor in Figure 41, which ranges from about 10^4 to 10^7. To increase Q_{TED} even further, we increase the plate thickness to 6 µm for the next iteration. The result can be seen in Figure 43.
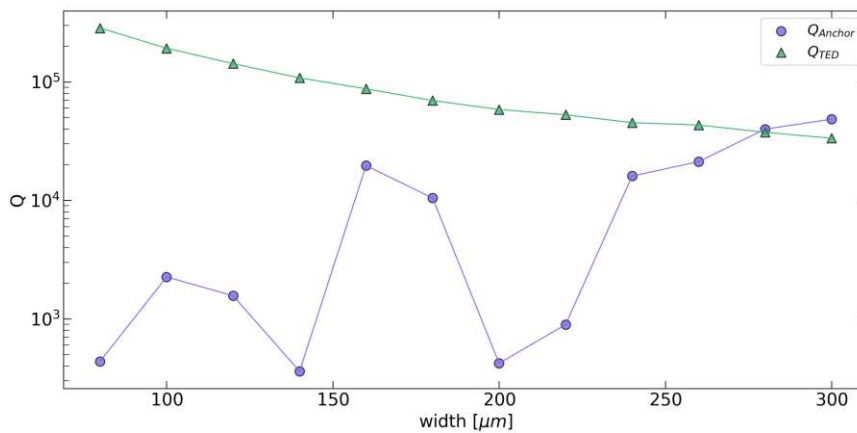
Figure 43: Quality factors for the 1:6 mode of a rectangular plate (L × W × H = 90 × 90 − 300 × 6 µm). The thermal limit is well above the anchor loss quality factor.

For the 6 µm plate, Q_{TED} is up to two orders of magnitude larger. However, the increase in thickness leads to a stiffer plate, which increases the resonance frequencies above the maximum measureable frequency of the measurement setup.

35

To lower the resonance frequencies, we increased the overall plate dimensions. Another FEM simulation featuring a larger plate (L×W×H = $200 \times 200 - 800 \times 15$ µm) yields resonance frequencies for the 1:6 mode below 24 MHz. In addition, Q_{TED} is up to two orders of magnitude larger than Q_{anchor}.
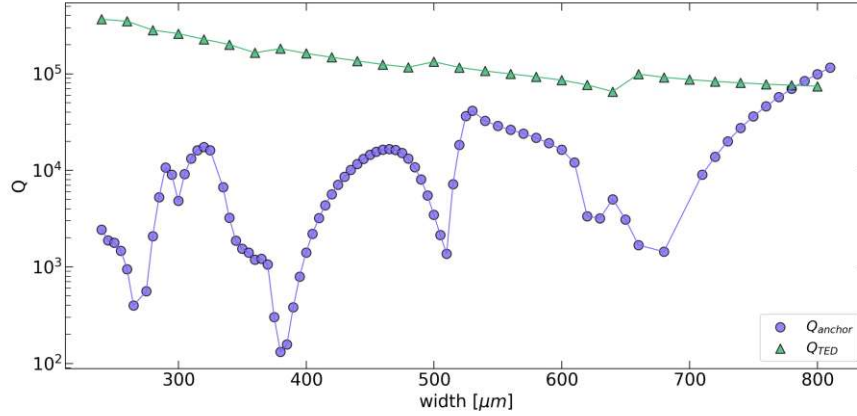
Figure 44: An increase in overall plate dimensions to $200 \times 200 - 800 \times 15$ µm, lifts Q_{TED} above the anchor loss related quality factor, while maintaining vibration frequencies below 24 MHz.

All previous simulation results has been carried out assuming an isotropic material (polycrystalline silicon). However, as the devices for experimental validation are fabricated from monocrystalline silicon[9] ($\rho = 2330$ kg m^{-2}) in (100) crystal orientation, the finite element model has to be modified accordingly. The elasticity matrix for the anisotropic material is [21]:

$$
E = \begin{pmatrix}
194.5 & 35.7 & 64.1 & 0 & 0 & 0 \\
35.7 & 194.5 & 64.1 & 0 & 0 & 0 \\
64.1 & 64.1 & 165.7 & 0 & 0 & 0 \\
0 & 0 & 0 & 79.6 & 0 & 0 \\
0 & 0 & 0 & 0 & 79.6 & 0 \\
0 & 0 & 0 & 0 & 0 & 50.9
\end{pmatrix} \text{GPa} \tag{14}
$$

The X, Y and Z axes of the simulation workspace correspond to the [110], [-110] and [100] directions of the silicon wafer.

Figure 45, shows simulation results for the same plate geometry as before, but for the anisotropic material:

---

[9]4-11176 SOI wafer from Ultrasil (`http://www.ultrasil.com/`)
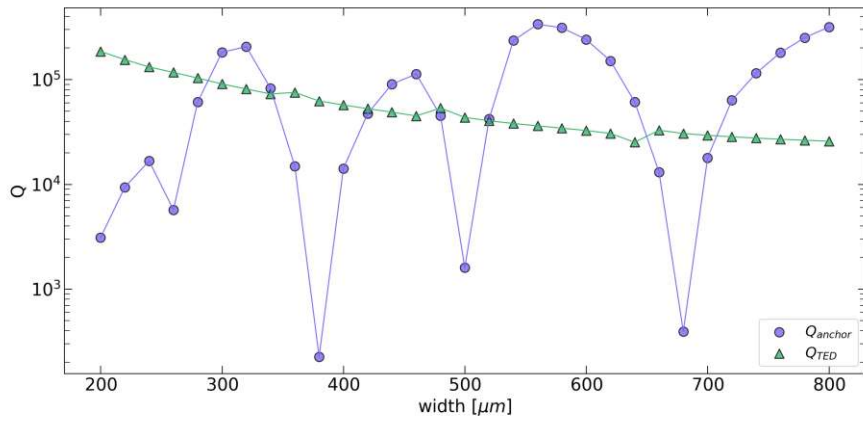
Figure 45: Q_{TED} and Q_{anchor}, again for the 1:6 mode of the $200 \times 200 - 800 \times 15$ µm plate, but this time for monocrystalline silicon in (100) crystal-configuration.

The relative difference between Q_{TED} and Q_{anchor} is smaller for monocrystalline silicon, as the new material yields a higher anchor-loss related quality factor. However, there are significant minima in Q_{anchor}, well below Q_{TED}. These minima should also be visible in the experimental quality factor measurements, since the minima in Q_{anchor} are still up to two orders of magnitude smaller than Q_{TED} at the same frequency.

4.3. Fabrication

The wafer of choice is a 4-11176 SOI wafer from *Ultrasil*[10]. SOI stands for silicon-on-insulator, where a layer of silicon oxide is buried at a certain depth. This layer acts as an etch-stop and separates the device layer from the substrate, which is called the handle layer. The properties of the wafer are listed in Table 5.

To fabricate the resonators, we carried out a standard BOSCH-process [22] (deep reactive-ion etching). The individual fabrication steps are illustrated in Figure 46. After covering the wafer with photoresist[11], a photolithography mask is brought in hard contact with the wafer and is then exposed to ultraviolet light (365 nm). As a next step, deep reactive ion etching is used to define the geometry of the plate resonators. After that, the backside of the wafer is treated the same way, and the handle layer is etched until the oxide layer is accessible from beneath. After removing the exposed oxide layer using hydrofluoric acid (HF), the plate resonators are released from the wafer.
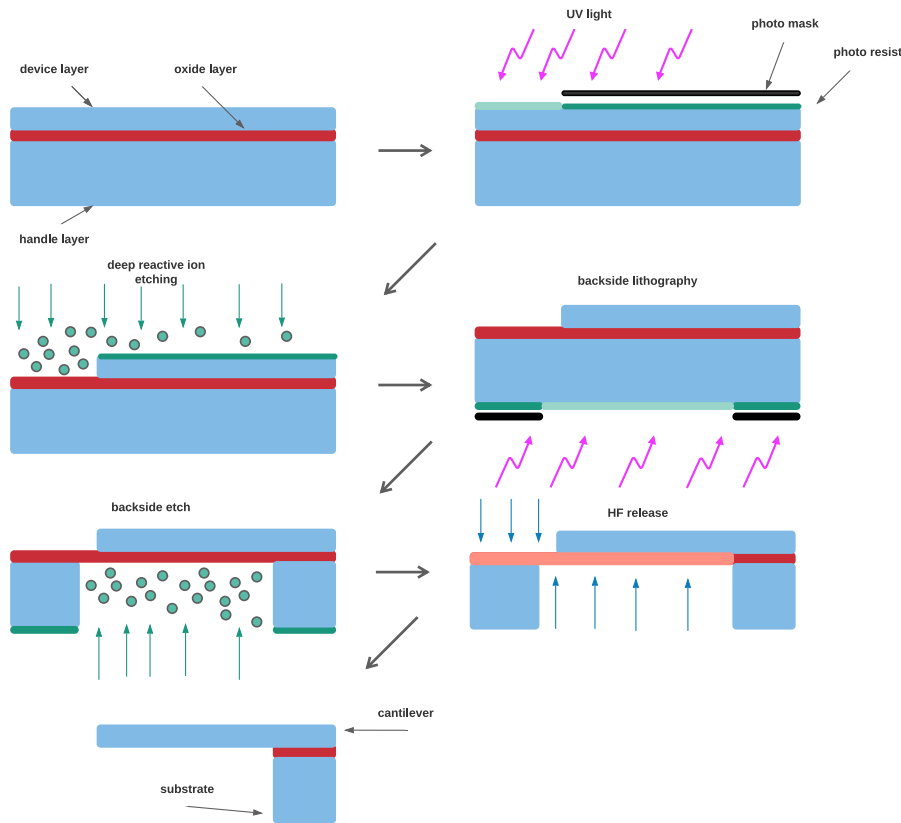
Figure 46: Individual fabrication steps using deep reactive ion etching.

---

[10]http://www.ultrasil.com/

[11]AZ5214 and AZ6624 from MicroChemicals. While the first layer of AZ5214 was used to align the plates, the second layer of AZ6624 was used for structuring. For the backside etch, two layers of AZ6624 were used.

Table 5: Properties of the used SOI-wafer.

Code	4-11176
Handle Material	Silicon
Doping type (handle)	n
Dopant (handle)	Sb
Doping type (device)	p
Dopant (device)	B
Res (Ohm cm)	<0.02
Finish (handle)	P (with 1 um oxide)
Finish (device)	P
Handle orientation	1-0-0
Handle thickness	400 +/- 10 um
Device thickness	15+/- 0.5 um

The photolithography mask for this project can be seen in Figure 47. The resonator width is altered from 200 µm to 800 µm, in increments of 3 µm. This leads to 200 different resonators in total. The individual silicon frames, where the resonators are attached to, have a length of 3 mm and a width of 1.5 mm.

(a) Complete Mask

(b) Close-up view
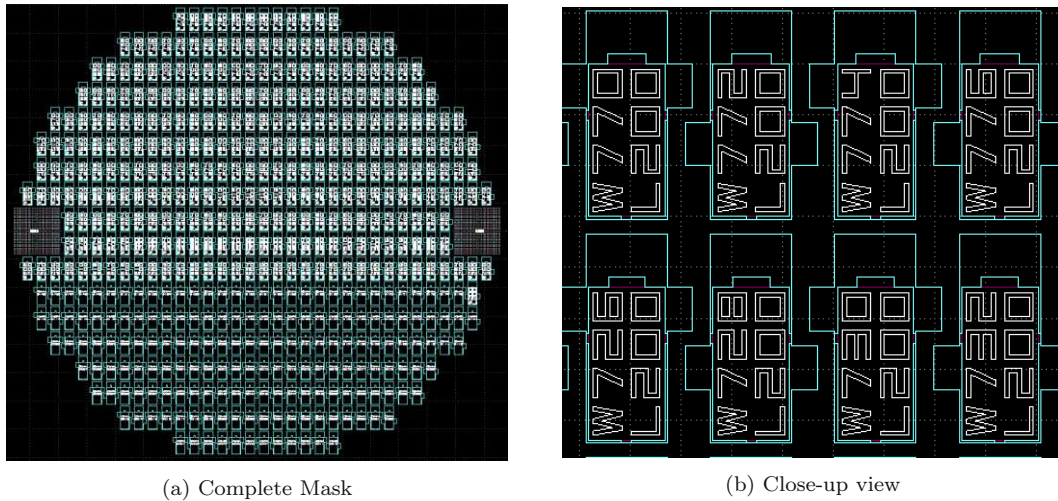
Figure 47: Lithography mask for the 200 fabricated plate resonators. Each resonator has a thickness of 15 µm and a length of 200 µm.

5. Experiments

This section describes the process to validate the effect of Q-factor oscillations for roof tile-shaped modes, which is described in section 3.3.

5.1. Measurement Setup

The Q-factor measurements are performed with a *Polytec* MSA-500[12] laser-doppler vibrometer in combination with an OFV-5000 vibrometer controller and an *Intermodulation Products* MLA-3[13] multifrequency lock-in amplifier.

The measurement setup is shown in Figure 48 and 49. All measurements are performed in vacuum ($< 2 \cdot 10^{-5}$ hPa). To excite the vibrational modes of interest, the resonators are placed on top of a piezo-actuator[14], using carbon tape[15].

(a) Single resonator chip

(b) Multiple chips placed on piezo-actuator
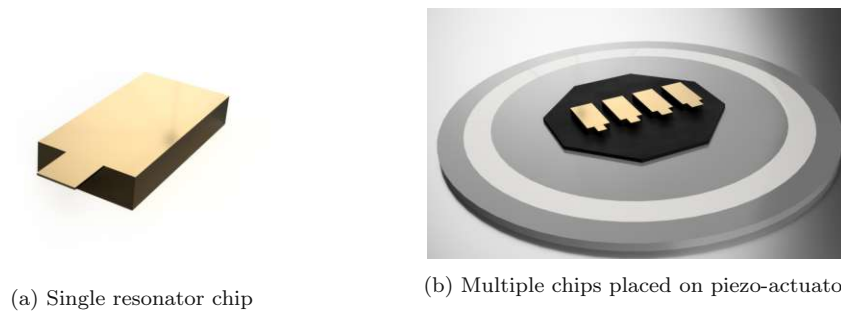
Figure 48: Each plate-resonator is attached to a substrate chip with 3 mm in length and 1.5 mm in width. For the measurement, multiple resonators are placed on top of a piezo-actuator, using carbon tape.

---

[12]https://www.polytec.com/fileadmin/d/Vibrometrie/OM_BR_MSA-500_E_42121.pdf

[13]https://intermodulation-products.com/support/technical-docs/_spec-sheets/mla3_spec_sheet_and_topology.pdf

[14]Piezo-actuator from PI Ceramics (https://www.physikinstrumente.store/eu/000014801/?c=65670).

[15]Carbon tape AGG3939 from Agrar Scientific.

Die approbierte gedruckte Originalversion dieser Diplomarbeit ist an der TU Wien Bibliothek verfügbar
The approved original version of this thesis is available in print at TU Wien Bibliothek.

TU Bibliothek
Your knowledge hub
WIEN
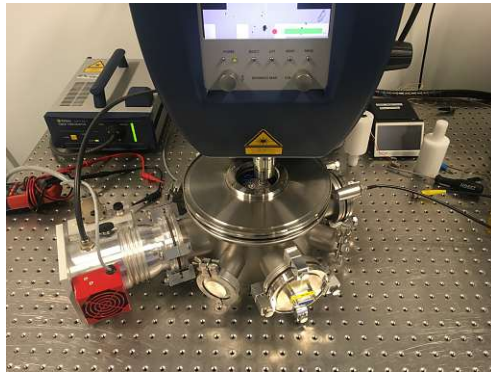
(a) MSA-500 Laser Doppler Vibrometer
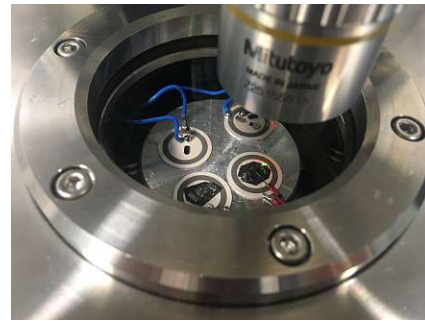
(b) Close-up view

Figure 49: Q-factor measurement setup. (a) shows the MSA-500 Laser-Doppler Vibrometer measuring through the window in the vacuum chamber. (b) shows a close-up look at the devices.

5.2. Measurement Protocol

To obtain the Q-factors, the following procedure has been performed for all devices:

1. The piezo-actuator is driven by the vibrometer controller, using the MSA-500 software. To excite as many modes simultaneously as possible, white noise with an amplitude of 1 V is used as input signal.

2. The Laser-Scanning-Mode of the MSA is used to identify the different mode shapes. In this mode, a rectangular, uniformly spaced grid is projected onto the resonator's top surface, and the displacement of every grid point is measured. The full mode shape of the plate is interpolated, using the measurements for any data point. Figure 50 shows an exemplary grid-scan of a 1:3 mode.
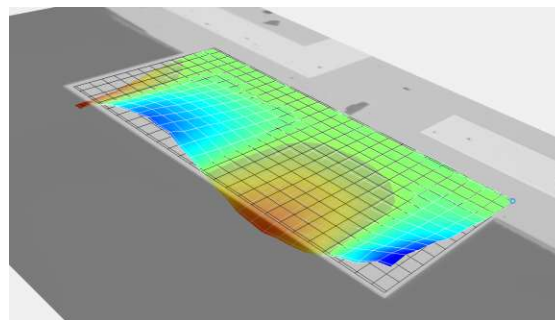
Figure 50: Exemplary grid-scan of the resonator surface (1:3 mode). Regions with maximum displacement are colored in blue, and regions with minimum displacement are colored in red.

3. All mode shapes of interest are selected by hand, and the corresponding resonance

frequencies are determined, using the graphical user interface of the MSA software. The resonance frequencies are stored in a text file.

4. The resonance frequencies are imported to a custom python script which controls the lock-in amplifier.

5. The laser spot is now placed on one corner of the plate. This ensures that we can observe all modes, as every mode has a non-zero displacement on the free end of the resonator during one cycle of vibration. The lock-in amplifier drives the piezo-actuator in the selected frequency-ranges and performs a fine sweep over the frequency intervals of interest.

6. A custom python script is used to fit a Lorentzian function to every resonance peak of interest. A sharp and narrow resonance peak indicates a high quality factor, while a broad peak indicates a low quality factor. This is illustrated with synthetic data in Figure 51.
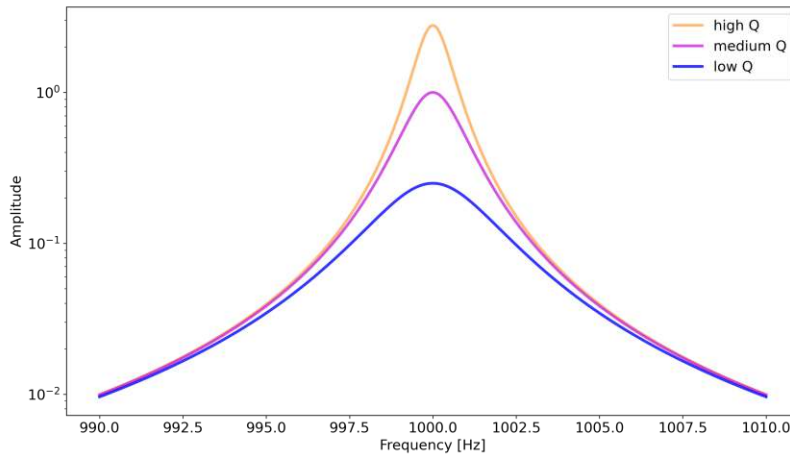
Figure 51: Synthetic data to illustrate resonance peaks with different quality factors at a resonance frequency of 1 kHz.

To determine the quality factor of a given frequency spectrum, a Lorentzian function is fitted to the data:

$$L(x) = \frac{a}{\gamma^2 + (\omega - \omega_0)^2} + b, \tag{15}$$

where ω_0 is the resonance frequency and a, b and γ are fitting parameters. As a Lorentzian-shaped function can also be derived from the harmonic oscillator's equation of motion, γ is directly related to the quality factor, as

$$Q = \frac{\omega_0}{2\,\gamma}. \tag{16}$$

An exemplary Lorentzian fit for the 1:3 Mode of a 440 µm wide plate can be seen in Figure 52.
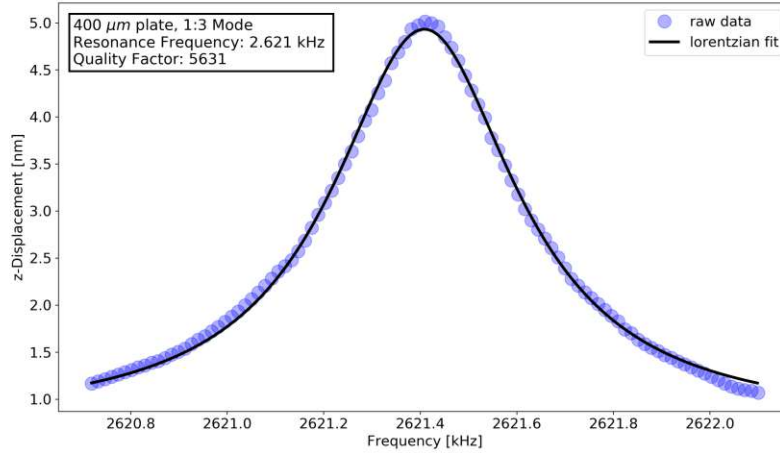
Figure 52: Example of a Lorentzian fit to determine the quality factor for the 1:3 mode for a plate width of 440 µm. The corresponding quality factor is 5631.

5.3. Results and Discussion

The modes 1:1 to 1:6 have been measured with the procedure described above, and the results are presented in the two following plots. The MSA-500 in combination with the DD-300 displacement decoder can measure frequencies up to 24 MHz. However, at frequencies above 10 MHz, it gets increasingly more difficult to identify the shape of a specific mode. This is the reason why the experimental data is restricted to plate widths above a certain threshold, dependent on the mode of interest (e.g. 240 µm for the 1:1 mode and 420 µm for the 1:6 mode). Below this threshold, a resonance peak cannot be easily assigned to a certain mode shape anymore, as the noise level is too high to reliably identify a mode by its displacement pattern.

In Figure 53, the experimental results are compared to the anchor-loss related quality factor and the thermoelastic quality factor. As different damping mechanisms contribute to the total quality factor of the system, we use Eq. 13 to calculate Q_{tot}.

Figure 54, shows the comparison between the experimental data and the total numerical quality factor. In both plots, the black line serves as a guide for the eye and is created by applying a Gaussian filter[16] with a σ parameter of 1.25 to the experimental data.

---

[16]https://docs.scipy.org/doc/scipy/reference/generated/scipy.ndimage.gaussian_filter1d

43
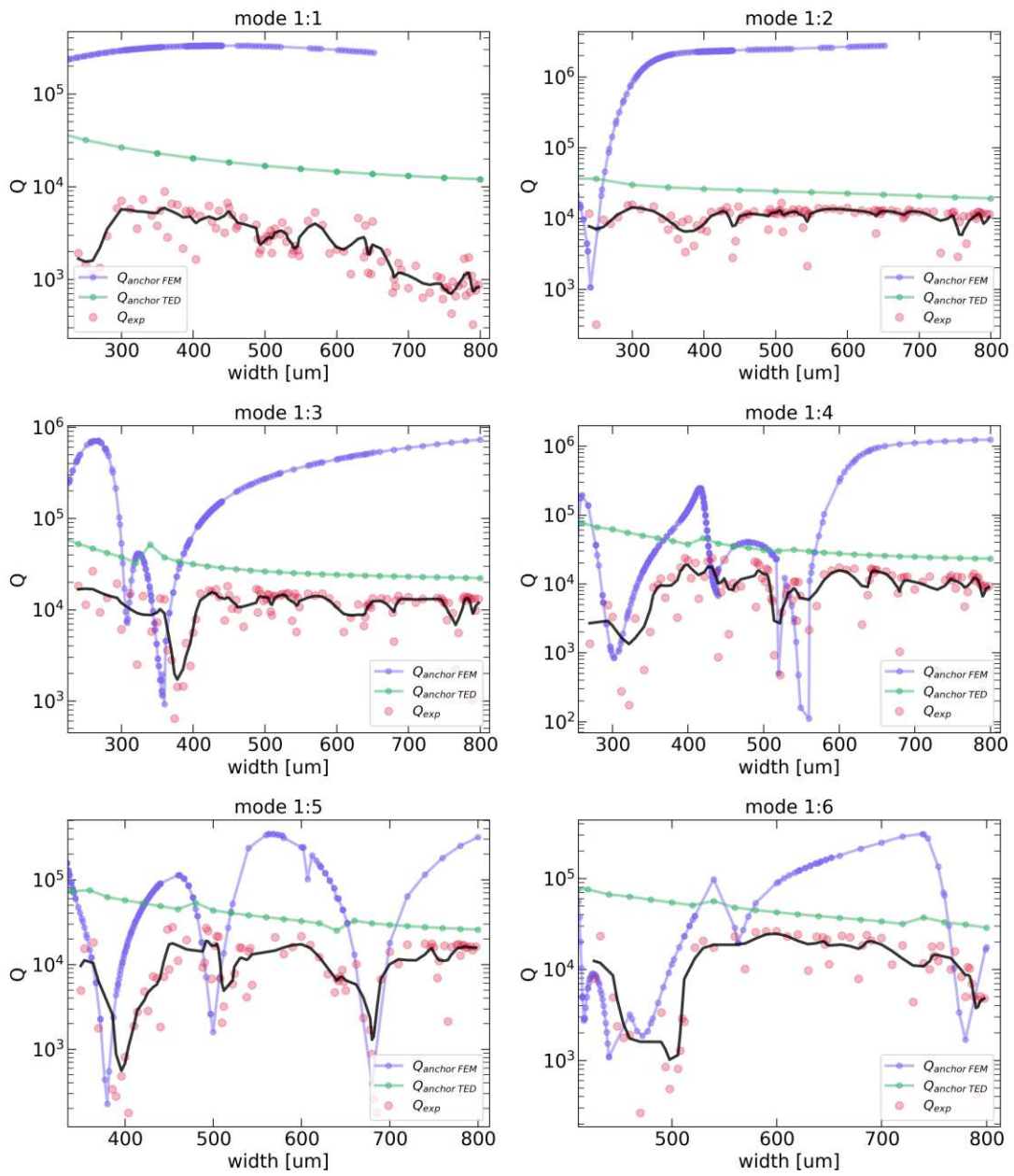
Figure 53: Comparison of experimental data with simulation results of anchor-loss related quality factor and thermoelastic quality factor. The black line serves as a guide for the eye and is created by applying a Gaussian filter ($\sigma = 1.25$) to the experimental data.
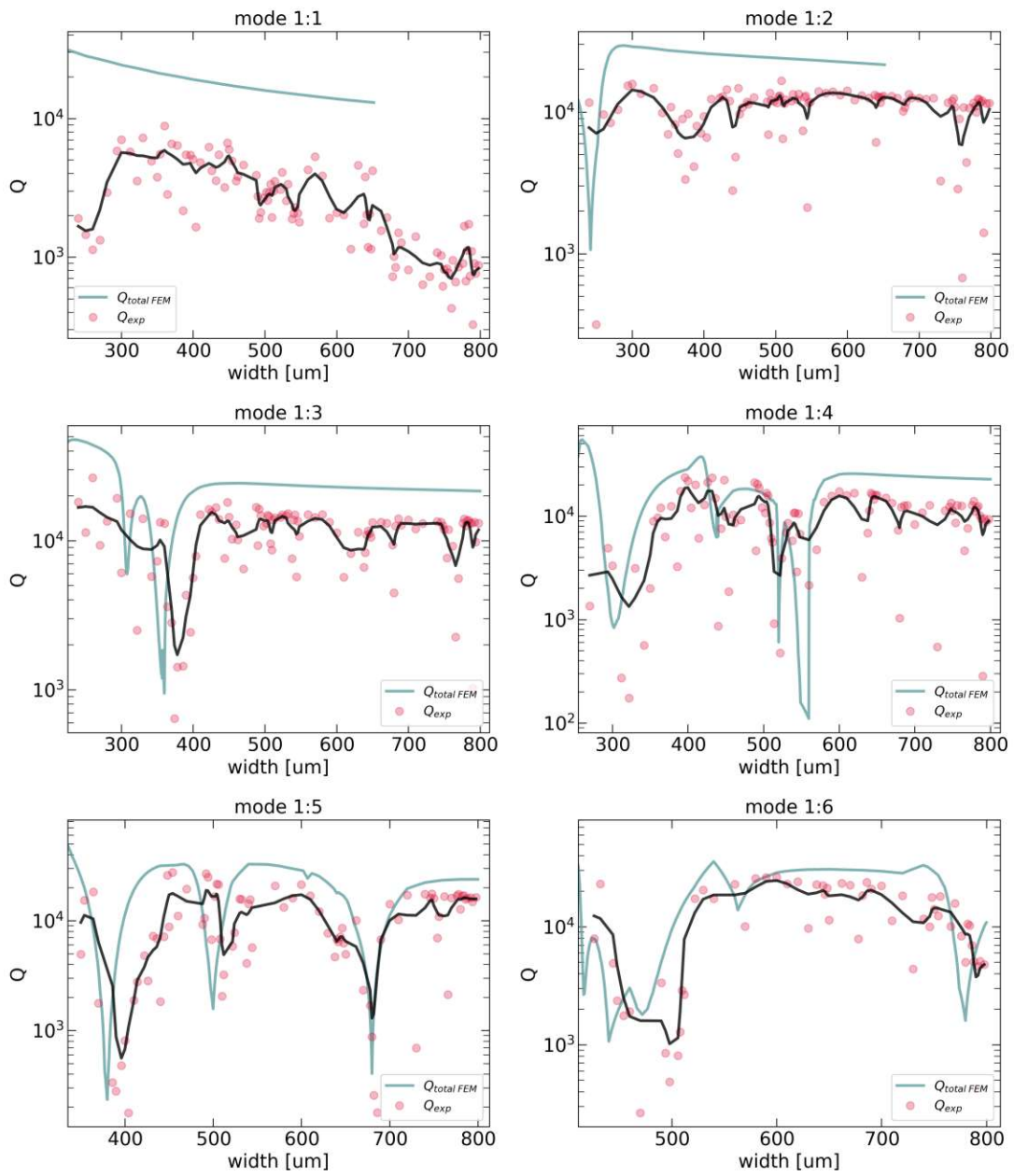
Figure 54: Comparison of experimental data with total quality factor obtained from the simulations. The black line serves as a guide for the eye and is created by applying a Gaussian filter ($\sigma = 1.25$) to the experimental data.

The simulations overestimate the quality factor in comparison with the experimental results. The average difference between simulation- and experimental results can be seen in Table 6.

Table 6: Average difference in quality factor between simulation- and experimental data.

mode	$Q_{\text{avg (FEM)}}$	$Q_{\text{avg (exp)}}$	absolute difference	relative difference [%]
1:1	19772.8	2779.5	16993.3	611.4
1:2	23096.6	10635.0	12461.6	117.2
1:3	23785.9	11295.1	12490.8	110.6
1:4	19713.7	10196.4	9517.3	93.3
1:5	21978.4	10634.3	11344.1	106.7
1:6	22429.5	12417.2	10012.4	80.6

The relative difference in average Q-factor ranges from 80-170 % for the modes 1:2 to 1:6, while the 1:1 mode has a relative difference of about 611 %. A reason for the relatively high difference for the 1:1 mode could be that there are no data points for plate widths above 670 µm. There are several possible explanations for the deviation between simulation- and experimental data. The simulation only takes into account the effects of anchor losses and thermoelastic damping. However, the *real* quality factor is a combination of various effects, where most of them are neglected in the model (e.g. losses due to internal- or surface friction, phonon-phonon interaction losses or medium losses due to remaining ballistic gas molecules [6]).

Most of the Q-factor minima in the simulation data can also be seen in the experimental data. This is especially the case for the modes 1:3, 1:5 and 1:6, where the quality factor shows very prominent dips, which are about one order of magnitude lower than the average quality factor. For the 1:2 mode, there is a single experimental data point indicating a possible minimum around 240 µm, which is present in the simulation results. Unfortunately, there is no more experimental data in this specific domain.

The observable minima are slightly shifted towards higher plate-widths in the experimental data. This indicates that the simulated resonance frequency is slightly higher than the resonance frequency in the measurement data. This can also be seen in Figure 55, where the resonance frequency is plotted against the plate-width.
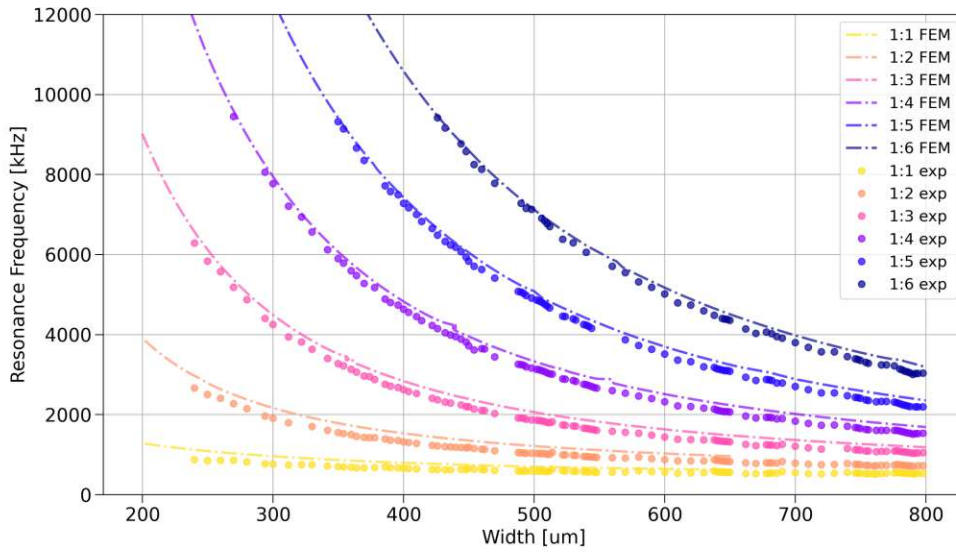
Figure 55: Comparison of the resonance frequency for the modes 1:1 to 1:6.

The measurements exhibit a notable level of fluctuations. This is expected, as quality factor measurements for high-Q resonators are known to be very sensitive to environmental parameters and the implementation of the measurement setup. Some possible explanations are:

1. According to the manufacturer of the wafer, the thickness of the device layer has a possible tolerance of +/- 0.5 µm. From our numerical study of Judge's estimation (see Figure 12), we already know that the anchor-loss related quality factor is very sensitive to changes in resonator thickness. The tolerance in thickness is usually not evenly distributed over the whole wafer, and can lead to differences in comparison with the numerical results. To estimate these deviations, we conducted a numerical error study for the 1:3 mode of a $200 \times 400 \times 15$ µm plate, by varying the thickness from 14.5 to 15.5 µm. The results are presented in Table 7. When assuming a nominal thickness of 15 µm, the resonance frequency varies about +/- 3.1 %. The deviations in quality factor are much higher, varying by about +/- 20 %. This is also consistent with the estimation by Judge [8], where the quality factor is dependent on the thickness of the resonator to the power of four (see Equation [5]).

Table 7: Numerical error study for the 1:3 mode of a $200 \times 400 \times 15$ µm plate. The plate thickness is varied from 14.5 to 15.5 µm.

thickness [µm]	f_{res} [kHz]	Q_{anchor}
14.5	2751	80362
15	2839	66920
15.5	2927	53443

2. Anchor losses are heavily dependent on the way the resonator chip (see Figure 48) is attached to the sample holder. In the presented measurements, the resonators are sticked to a piezo actuator using double-sided carbon tape, which is again sticked to a stainless steel socket in the vacuum chamber. The layer of carbon tape is relatively soft and should therefore act as a barrier for elastic waves between the substrate and the environment. However, as the quality of the connection varies for each resonator which is sticked to the carbon tape, it is expected to have significant influence on the quality factor.

3. The top surface of some chips is slightly scratched due to the release out of the wafer. This could influence the propagation of waves close to the surface, which are expected to have a major impact on the quality factor.

4. The substrate-chip has a rectangular footprint of 3 mm length and 1.5 mm width. This could possibly cause issues for modes with lower resonance frequency, as the wavelength is larger than the substrate dimensions. This is illustrated in Figure 56. Figure 56a shows our design we used for the experiments. For future measurements, it could make sense to design a larger substrate (Figure 56b), to ensure that the wavelength is smaller than the dimensions of the substrate. A step beyond could be a substrate with a circular footprint (Figure 56c), which could help to minimize reflections on the edges and corners of the substrate.

(a) Our design.

(b) Design with larger substrate.

(c) Design with spherical substrate.
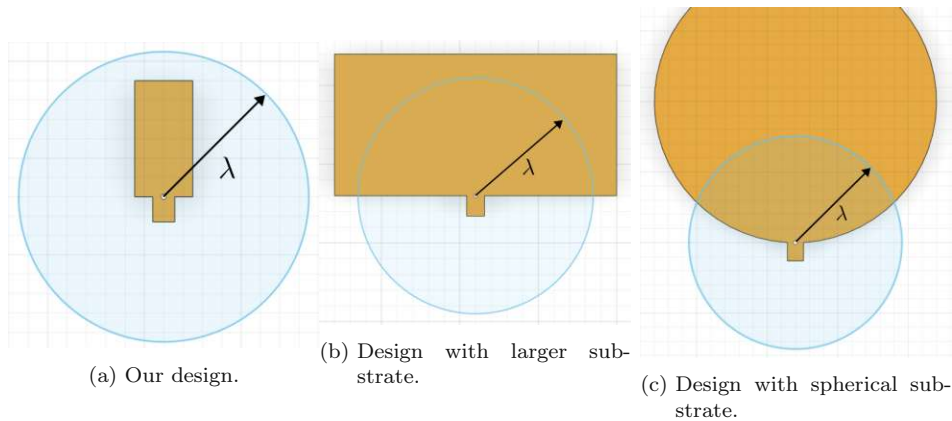
Figure 56: Comparison of different substrate geometries. λ denotes the wavelength for each mode of vibration. Dimensions are not to scale.

When assuming a silicon speed of sound of 5092 m/s [13], a resonance frequency of at least 6.75 MHz is required to get a wavelength below 0.75 mm, which is half the width of the substrate chip. The only modes with a significant amount of data points above this frequency are the 1:5 mode below 414 µm and the 1:6 mode below 510 µm. These data points however, seem not to behave any different from the data points with frequencies below 6.75 MHz. This indicates that the effect is possibly neglectable, but as there are not that many comparable data points this is not entirely sure.

5. The cause of some outliers has been identified as failed Lorentzian fits. This can usually happen when two resonance peaks are very close to each other, and the fitting algorithm tries to fit the Lorentzian function to a double-peak. All outliers due to failed fits have been removed from the plots.

6. Conclusions and Outlook

We investigated how the quality factor of plate resonators changes with different plate widths. We performed finite-element simulations for multiple two-dimensional vibrational modes of thin plates, with a focus on so-called roof tile-shaped modes. We designed a finite-element model using a perfectly matched layer (PML), and validated our model against analytical solutions. We have shown, that the damping effect of anchor losses in MEMS resonators is highly dependent on the specific shape (displacement distribution) of the modes.

For the energy transportation in the substrate, antisymmetric modes (modes with an odd number of nodal lines) form characteristic symmetric side lobes. For symmetric modes, the mechanical energy flux is mostly split into two parts, where one part is emitted close to the surface, and the other part is forming a concentrated lobe downwards into the substrate.

Additionally, we observed a modulation of the quality factor of up to two orders of magnitude for 2D plate modes, dependent on the width and mode order of the plate. This is exactly the effect we have been looking for, as it confirms our hypothesis (see Section 1) that the force distribution in the anchor region can act as a combination of point sources of elastic energy, which can interfere with each other. This interference effect is similar to the effect observed in numerical studies of silicon micro-pillar resonators [13] [23]. The period width of the oscillations in the quality factor is decreasing for higher mode orders, where the ratio between plate width and wavelength[17] is in the same order of magnitude.

To observe this modulation, it is important to keep thermoelastic losses low. We accomplished this by increasing the overall plate dimensions, as suggested by Roszhart's [24] estimation. If this is not possible, it could help to cool down the resonator, as the thermoelastic Q-factor has an inverse proportional dependency on the temperature. However, for some resonator geometries, Q_{TED} is at least one order of magnitude lower than Q_{anchor} (see Figure 41). To see a notable effect, it would require sophisticated cooling solutions using liquid helium.

For experimental validation, we designed and fabricated 200 plate resonators using deep reactive ion etching. To determine the quality factor, we used Laser-Doppler vibrometry and confirmed that the predicted Q-factor oscillations can also be measured in the experiment. The experimental data exhibits notable fluctuations, which is expected, as high Q measurements are known to be very susceptible to environmental parameters and variations in the measurement setup. To estimate the deviations in Q which are caused by nonuniform wafer thickness, we conducted a numerical error study. When the thickness of the resonator is varied in a range of the manufacturer's tolerance, the quality factor can deviate by about +/- 20 %.

Nevertheless, the experimental data shows a high level of accordance with the simulation results. This is especially visible for the modes 1:3, 1:5 and 1:6.

---

[17]The wavelength λ is estimated by dividing the phase velocity v (estimated 5092 m/s [13]) by the resonance frequency f.

Anchor losses are one of the dominating damping effects for high-Q resonators in vacuum. The mode-dependent modulation of the quality factor for plate resonators is therefore an important finding, which could help to increase the level of control over the performance of the resonator.

A possible future use case could be a precise coupling of different resonators attached to the same substrate, utilizing the mode-specific spatial footprint of energy flow in the substrate. This could also act as a sort of acoustic shielding, where interference effects caused by one resonator increase the quality factor of another resonator by shielding it off due to destructive interference.

This is a very different approach to previous methods, as it does not require any special changes to the anchor design, like phononic crystals [12], or making sure to only support the resonators on points where a nodal line touches the anchor.

To fully understand the possible potential of this mechanism, additional research is needed. A starting point for future studies could be the quantification of the three-dimensional energy flow in the substrate. Additionally, as stated in Section 5.3, future resonator designs could make use of a larger substrate with a circular footprint, which may improve the resonator performance.

References

[1] G. Binnig, C. F. Quate, and Ch. Gerber. Atomic force microscope. *Phys. Rev. Lett.*, 56:930–933, Mar 1986.

[2] Sang-Gook Kim, S.Jeba Priya, and Isaku Kanno. Piezoelectric mems for energy harvesting. *MRS Bulletin*, 37, 11 2012.

[3] Isabelle Etchart, Hua Chen, Philip Dryden, Jacques Jundt, Christopher Harrison, Kai Hsu, Frederic Marty, and Bruno Mercier. Mems sensors for density–viscosity sensing in a low-flow microfluidic environment. *Sensors and Actuators A: Physical*, 141(2):266–275, 2008.

[4] Nam-Trung Nguyen, Xiaoyang Huang, and Toh Kok Chuan. MEMS-Micropumps: A Review . *Journal of Fluids Engineering*, 124(2):384–392, 05 2002.

[5] A. Einstein. Über die von der molekularkinetischen Theorie der Wärme geforderte Bewegung von in ruhenden Flüssigkeiten suspendierten Teilchen [adp 17, 549 (1905)]. *Annalen der Physik*, 14(S1):182–193, 2005.

[6] Silvan Schmid, Luis Guillermo Villanueva, and Michael Lee Roukes. *Fundamentals of Nanomechanical Resonators.* Springer, Berlin, Heidelberg, 2016.

[7] D.B. Leeson. A simple model of feedback oscillator noise spectrum. *Proceedings of the IEEE*, 54(2):329–330, 1966.

[8] John Judge, Douglas Photiadis, Joseph Vignola, Brian Houston, and Jacek Jarzynski. Attachment loss of micromechanical and nanomechanical resonators in the limits of thick and thin support structures. *Journal of Applied Physics*, 101:013521–013521, 01 2007.

[9] I. Wilson-Rae. Intrinsic dissipation in nanomechanical resonators due to phonon tunneling. *Physical. Review. B*, 77:245418, Jun 2008.

[10] A. Frangi, A. Bugada, M. Martello, and P.T. Savadkoohi. Validation of PML-based models for the evaluation of anchor dissipation in mems resonators. *European Journal of Mechanics - A/Solids*, 37:256–265, 2013.

[11] S.Y. Chen, J.Z. Liu, and F.L. Guo. Evaluation of support loss in micro-beam resonators: A revisit. *Journal of Sound and Vibration*, 411:148–164, 2017.

[12] R Olsson and Ihab El-Kady. Microfabricated phononic crystal devices and applications. *Measurement Science and Technology*, 20:012002, 11 2008.

[13] S. Schmid H. Kaehler and D. Platz. Wave coupling between mechanical resonators in the MHz regime. *In Print*, 2020.

[14] A. Hrennikoff. Solution of Problems of Elasticity by the Framework Method. *Journal of Applied Mechanics*, 8(4):A169–A175, 03 2021.

[15] R. Courant. Variational methods for the solution of problems of equilibrium and vibrations. *Bulletin of the American Mathematical Society*, 49(1):1 – 23, 1943.

[16] Jean-Pierre Berenger. A perfectly matched layer for the absorption of electromagnetic waves. *Journal of Computational Physics*, 114(2):185–200, 1994.

[17] Frank D. Hastings, John B. Schneider, and Shira L. Broschat. Application of the perfectly matched layer (PML) absorbing boundary condition to elastic wave propagation. *The Journal of the Acoustical Society of America*, 100(5):3061–3069, 1996.

[18] A.W. Leissa. The free vibration of rectangular plates. *Journal of Sound and Vibration*, 31(3):257–293, 1973.

[19] Brian Mace and Elisabetta Manconi. Mode veering in coupled continuous systems. *20th International Congress on Sound and Vibration 2013, ICSV 2013*, 4:3153–3160, 01 2013.

[20] COMSOL. *The structural mechanics module user's guide.* COMSOL, 1998-2018.

[21] M. A. Hopcroft, W. D. Nix, and T. W. Kenny. What is the young's modulus of silicon? *Journal of Microelectromechanical Systems*, 19(2):229–238, 2010.

[22] Schilp Andrea (Schwabisch Gmund) Laermer, Franz (Stuttgart). Method of anisotropically etching silicon, March 1996.

[23] Michael V. Berry, John T. Foley, Greg Gbur, and Emil Wolf. Nonpropagating string excitations. *American Journal of Physics*, 66:121–123, 1998.

[24] T. V. Roszhart. The effect of thermoelastic internal friction on the q of micromachined silicon resonators. In *IEEE 4th Technical Digest on Solid-State Sensor and Actuator Workshop*, pages 13–16, 1990.

[25] E.M. Lifshitz, A.M. Kosevich, and L.P. Pitaevskii. Chapter ii - the equilibrium of rods and plates. In E.M. Lifshitz, A.M. Kosevich, and L.P. Pitaevskii, editors, *Theory of Elasticity (Third Edition)*, pages 38–86. Butterworth-Heinemann, Oxford, third edition edition, 1986.

[26] S. Timoshenko. *History of Strength of Materials: With a Brief Account of the History of Theory of Elasticity and Theory of Structures*. Dover Civil and Mechanical Engineering Series. Dover Publications, 1983.

[27] E.M. Lifshitz, A.M. Kosevich, and L.P. Pitaevskii. Chapter i - fundamental equations. In E.M. Lifshitz, A.M. Kosevich, and L.P. Pitaevskii, editors, *Theory of Elasticity (Third Edition)*, pages 1–37. Butterworth-Heinemann, Oxford, third edition edition, 1986.

List of Figures

List of Tables

A. Appendices

A.1. Euler-Bernoulli Beam Theory

For the fundamental bending modes of slendered, beam shaped structures, analytic solutions have been derived by Leonard Euler and Daniel Bernoulli [25] [26].

We make the following assumptions for a beam with length l and thickness h:

1. The beam is *slim*, which means $l/h > 10$.

2. Cross-sectional areas of the beam, which are perpendicular to the beam's axis before deflection, are also perpendicular to the beam's axis after deflection. This is Bernoulli's first hypothesis.

3. Cross-sectional areas of the beam stay even during deflection. This is Bernoulli's second hypothesis.

4. Deflections $u(x)$ are small in comparison to the length l of the beam.

5. The beam is made of isotropic material and follows Hooke's law.

When we neglect rotational inertia and shear deformation, the equation of motion for small displacements $u(x,t)$ is:

$$\rho A \frac{\partial^2 u(x,t)}{\partial t^2} + EI \frac{\partial^4 u(x,t)}{\partial x^4} + q(x) = 0, \tag{17}$$

where ρ is the mass density, A is the cross-sectional area, E is the Young's modulus and I denotes the moment of inertia. The additional term $q(x)$ describes external loads on the beam. In the absence of an external transverse load (q=0), the equation describes a free, vibrational motion of the beam.

Assuming a superposition of harmonic oscillations, the following ansatz

$$u_n(x,t) = e^{i\omega_n t}\, \phi_n(x), \quad n \in \mathbb{N} \tag{18}$$

yields

$$EI \frac{\partial^4 \phi_n(x)}{\partial x^4} - \rho A\, \omega_n^2\, \phi_n = 0 \tag{19}$$

where ω_n denotes the frequency of vibration. A general solution of 19 is:

$$u_n(x) = A_1 \cosh(\beta_n x) + A_2 \sinh(\beta_n x) + A_3 \cos(\beta_n x) + A_4 \sin(\beta_n x), \tag{20}$$

with

$$\beta_n(\omega_n) = \left(\frac{\rho A \omega_n^2}{EI} \right)^{\frac{1}{4}} \tag{21}$$

and ω_n being the natural frequency of each mode of vibration. The coefficients A_1-A_4 are constants which are determined by the problem's boundary conditions.

Table 8: Boundary conditions for a cantilevered beam of length l, which is clamped at x=0.

	u_n	$\frac{du}{dx}$	$\frac{d^2u}{dx^2}$	$\frac{d^3u}{dx^3}$
x = 0	0	0		
x = l			0	0

Applying the boundary conditions for a beam of length l which is clamped at x=0 (see Table 8), leads to the following equation:

$$\cosh(\beta_n l)\cos(\beta_n l) - 1 = 0, \tag{22}$$

which can be solved using numerical methods.

The first non-trivial solutions are:

1. $\beta_1 l = 1.87509$

2. $\beta_2 l = 4.73004$

3. $\beta_3 l = 7.85320$

4. $\beta_4 l = 10.9956$

Plugging these solutions in Eq. 20 and Eq. 21, the natural frequency ω_n and the corresponding mode shape $u_n(x)$ can be determined for each mode n. The first four mode shapes of a cantilevered beam of length l=1 are shown in Figure 57:
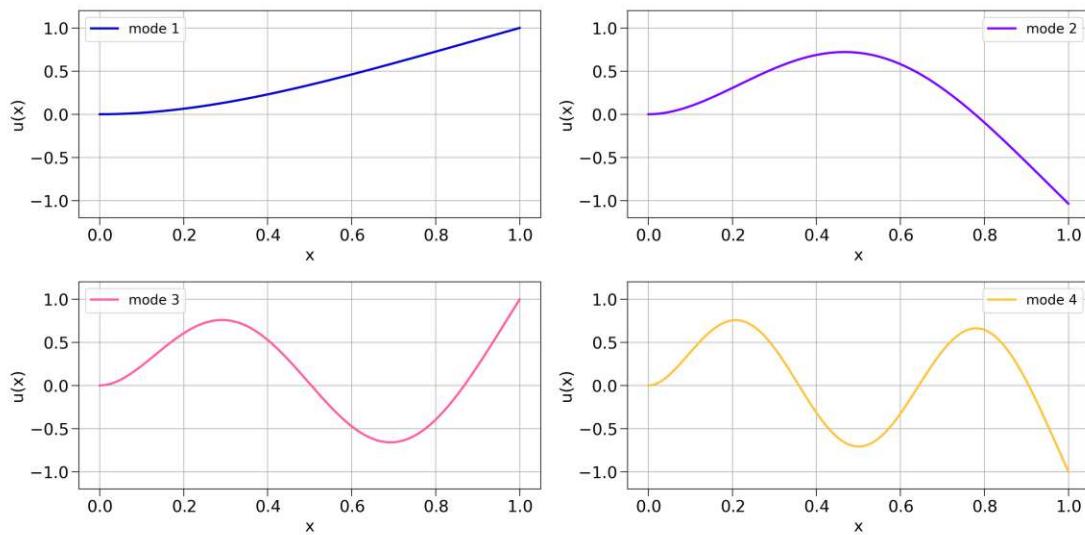

Figure 57: Analytical solutions for the first four mode shapes of an Euler-Bernoulli beam with length l=1.

A.2. Lumped-Element Model

If resonators are driven in the linear regime, the continuum mechanical relation between stress σ and strain ϵ is

$$\sigma_{ij} = C_{ijkl}\,\epsilon_{kl} \tag{23}$$

where C_{ijkl} denotes the material's elasticity tensor [27]. This is usually the case for small vibration amplitudes. As a consequence, the resonator can be approximated as a simple 1D harmonic oscillator model.

A harmonic oscillator can be interpreted as a spring-mass-model, as shown in Figure 58, where m is the mass, k is the spring constant and c is the damping constant.
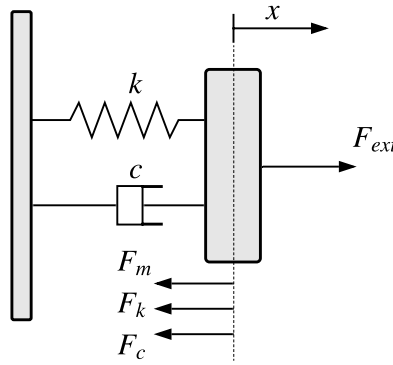

Figure 58: Harmonic Oscillator Model

An external force F_{ext} causes a displacement x of the mass out of its equilibrium position at $x = 0$.

In the linear regime, the spring causes a force F_k proportional to x (Hooke's law):

$$F_k = -kx \tag{24}$$

Due to Newton's second law, F_k causes a force in the opposite direction:

$$F_m = m\ddot{x} \tag{25}$$

The damping element with the damping constant c causes a damping force F_c, which is proportional to the negative velocity $\dot{x}$:

$$F_c = -c\dot{x} \tag{26}$$

The force balance yields:

$$F_m + F_k + F_c = F_{\text{ext}} \tag{27}$$

In the absence of an external force F_{ext} the system is described by homogenous second order differential equations:

$$m\ddot{x} + c\dot{x} + kx = 0 \tag{28}$$

With the definition of the natural frequency $\omega_0 = \sqrt{k/m}$ and the damping ratio $\zeta = \frac{c}{2\sqrt{mk}}$, Equation 28 can be rewritten as:

$$\ddot{x} + 2\zeta\omega_0\dot{x} + \omega_0^2 x = 0 \tag{29}$$

The damping in the system can also be characterized by the quality factor Q, which is defined as the ratio of the energy stored in the system, and the energy dissipated per vibration cycle:

$$Q = 2\pi \cdot \frac{W}{\Delta W}. \tag{30}$$

With

$$Q = \frac{1}{2\zeta} = \frac{\sqrt{mk}}{c}, \tag{31}$$

equation 29 can be written as

$$\ddot{x} + \frac{\omega_0}{Q}\dot{x} + \omega_0^2 x = 0. \tag{32}$$

Q is inversely proportional to the width of the resonance peak and increases the vibrational amplitude at resonance.

A.3. Laser-Doppler Vibrometry

A Laser-Doppler vibrometer is essentially an interferometer with two beam paths. The operating principle is illustrated in Figure 59. The object beam (which is projected onto the object of interest) experiences a frequency shift due to the Doppler effect while it is reflected on a moving surface. The reflected beam gets merged with a reference beam (without frequency shift) and the intensity of the combined beam is measured by a photodetector (commonly a photo diode).
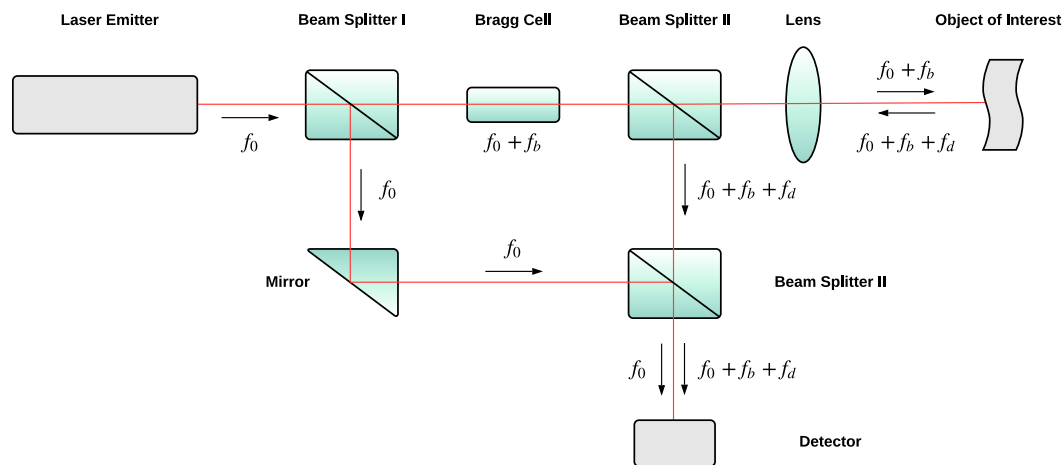

Figure 59: Operating principle of Laser-Doppler Vibrometry

The velocity of the moving object is directly proportional to the frequency shift of the object beam and can be written as

$$v(t) = \frac{f_d \cdot \lambda_{\text{laser}}}{2}, \tag{33}$$

where f_d is the Doppler-shift and λ_{laser} is the wavelength of the detected laser beam.

Since both an extension and a shortening of the object beam path caused by motion of the object under test produces the same frequency shift, the movement direction of the object cannot be uniquely recognized with this setup alone.

For this purpose, an acousto-optic modulator[18] (AOM) is placed in the reference beam path, which causes a shift in the laser frequency. In this way, a specific modulation frequency of the interference pattern is generated, which indicates that the measurement object does not move.

This modulation frequency is increased, if the object moves towards the interferometer, and decreased if it moves away from the interferometer. This makes it possible to clearly determine not only the absolute value of the velocity, but also the direction of movement.

To measure displacement, the velocity signal is integrated. In the frequency domain, the following relation can be used for integration

$$v = 2\pi \cdot f \cdot s, \tag{34}$$

where f is the frequency, v is the velocity of the object and s denotes the displacement at a specific frequency.

The displacement can also be directly obtained using another procedure which counts the transitions between light and dark in the interference pattern:

$$s = \frac{\lambda_{laser}}{2} \cdot n, \tag{35}$$

where n is the number of interference maxima.

---

[18]Acousto-optic modulators are based on the variation of the refractive index of a medium due to the presence of sound waves. These variations in the refractive index, cause variations in light waves by refraction, diffraction, and interference effects.

A.4. Thermoelastic Losses

Thermoelastic losses are caused by internal friction in a vibrating structure. During one cycle of vibration, regions under tensile stress are cooled down while regions under compressive stress are heated up. The induced temperature gradient leads to irreversible heat flow and causes vibrational energy to be dissipated.
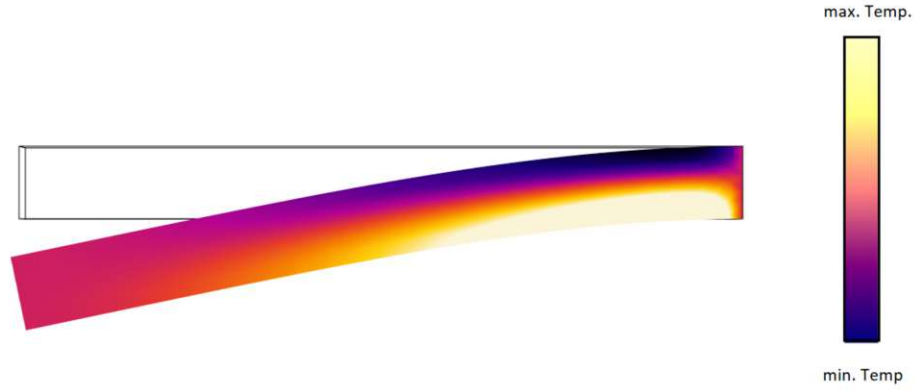

Figure 60: Illustration of thermoelastic damping for a beam vibrating in its first fundamental bending mode. Regions under tensile stress are cooled down, while regions under compressive stress are heated up.

Assuming a slender beam vibrating in one of its flexural modes, Roszhart et al. [24] proposed the following analytical estimation for the quality factor

$$Q = \frac{1}{2\,\Gamma(T)\,\Omega(f)}, \tag{36}$$

with the temperature-dependent function

$$\Gamma(T) = \frac{\alpha^2\,T\,E}{4\,\rho\,C_p}, \tag{37}$$

the frequency-dependent function

$$\Omega(f) = \frac{2\,f_0\,f}{f_0^2 + f^2}, \tag{38}$$

and the characteristic damping frequency of the cantilever

$$f_0 = \frac{\pi\,K}{2\,\rho\,C_p\,t_c^2}, \tag{39}$$

where:

T: cantilever temperature
E: Young's modulus
C_p: heat capacity under constant pressure
ρ: cantilever density
α: thermal expansion coefficient
K: thermal conductivity
f: cantilever frequency
t_c: cantilever thickness